

# Diamond-to-graphite transformation under hypersonic impact

Abhijit Biswas<sup>\*1</sup>, Aniket Mote<sup>2</sup>, Rajib Sahu<sup>3</sup>, Marcelo Lopes Pereira Junior<sup>1,4</sup>, Shuo Yang<sup>5</sup>, Sudaice Kazibwe<sup>6</sup>, Jishnu Murukeshan<sup>1</sup>, Raphael Benjamin de Oliveira<sup>1</sup>, Guilherme da Silva Lopes Fabris<sup>7</sup>, Shreyasi Chattopadhyay<sup>1</sup>, Gelu Costin<sup>8</sup>, Jianhua Li<sup>9</sup>, Robert Vajtai<sup>1</sup>, Ching-Wu Chu<sup>6</sup>, Lihong Lang<sup>10</sup>, Yu Zou<sup>10</sup>, Liangzi Deng<sup>6</sup>, Tobin Filletter<sup>5</sup>, Douglas Soares Galvão<sup>7</sup>, Christian Kübel<sup>3,11</sup>, Thomas E Lacy Jr<sup>2</sup>, and Pulickel M. Ajayan<sup>\*1</sup>

## AFFILIATIONS

<sup>1</sup>Department of Materials Science and Nanoengineering, Rice University, Houston, TX, 77005, USA

<sup>2</sup>J. Mike Walker '66 Department of Mechanical Engineering, Texas A&M University, College Station, TX 77843, USA

<sup>3</sup>Karlsruhe Nano Micro Facility (KNMF) & Institute of Nanotechnology (INT), Karlsruhe Institute of Technology (KIT), Kaiserstr. 12, 76131 Karlsruhe, Germany

<sup>4</sup>College of Technology, University of Brasília, Brasília, DF, 70910-900, Brazil

<sup>5</sup>Department of Mechanical & Industrial Engineering, University of Toronto, 5 King's College Road, Toronto, M5S 3G8, Canada

<sup>6</sup>Department of Physics and Texas Center for Superconductivity (TcSUH), University of Houston, Houston, TX, 77004, USA

<sup>7</sup>Applied Physics Department and Center for Computational Engineering & Sciences, State University of Campinas, Campinas, SP, 13083-970, Brazil

<sup>8</sup>Department of Earth, Environmental and Planetary Sciences, Rice University, Houston, TX, 77005, USA

<sup>9</sup>Shared Equipment Authority, Rice University, Houston, TX, 77005, USA

<sup>10</sup>Department of Materials Science and Engineering, University of Toronto, 5 King's College Road, Toronto, M5S 3G8, Canada

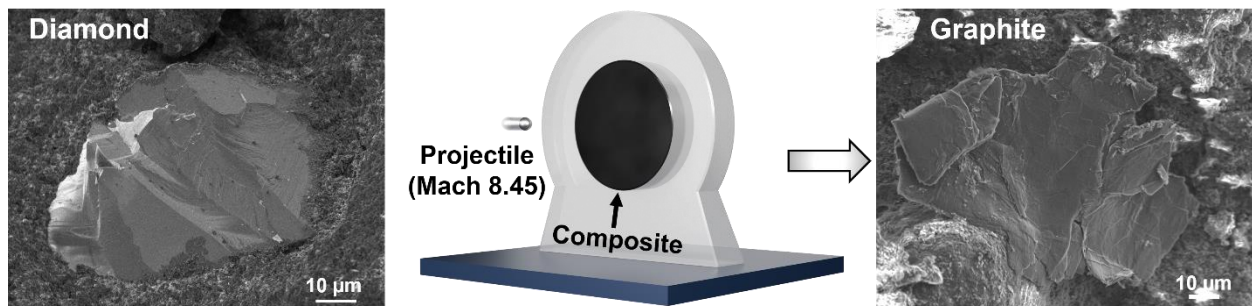
<sup>11</sup>Institute of Materials Science, Technical University Darmstadt (TUDa), Peter-Grünberg-Str. 2, 64287 Darmstadt, Germany

\*Corresponding authors: **abhijit.biswas@rice.edu; ajayan@rice.edu**

A. Mote, R. Sahu, and M. L. Pereira Junior contributed equally to this work.

## Abstract

Diamond-to-graphite transformation is a complex kinetically driven process which has been studied under various conditions for its fundamental importance. We report the transformation of diamond embedded ceramic matrix composites during hypersonic impact. Diamond particles embedded in cubic boron nitride matrix provide a superhard composite that was subjected to high impact collisions of metal projectiles travelling at speeds reaching Mach 8.45. Our observations suggest that the energy absorption and fracture of the composite is primarily enabled via the phase change of diamond into graphite. Characterization of the impact-fractured composite shows transformed diamond particles and provides details of the shock-induced phase transformation and the nature of diamond-graphite interfaces formed during rapid phase change. The study provides new understanding of phase transformation of diamond under extreme conditions.



**Keywords:** Diamond, composite, hypersonic impact, graphite, phase transformation

## Introduction

Diamond, the hardest known material, possesses exceptional mechanical (1, 2) and thermal properties (3), making it indispensable for extreme condition applications (4, 5). For advanced industrial use, scalable production of diamond and diamond-based composites is necessary and is mostly achieved through vapor phase deposition of diamond coatings or high pressure, high temperature methods (6–10). Scalable synthesis and stabilization of diamond and diamond-based composites via consolidation of diamond micro-powders would be extremely useful but remains challenging (6, 11, 12), as diamond is susceptible to graphitization at elevated sintering temperatures (13–16). One approach, as yet unexplored, for the synthesis of diamond-based composites would be to use structurally and functionally compatible materials, such as cubic boron nitride (cBN) (17, 18) as the matrix and well-known stabilizers for diamond synthesis such as transition-metals (19, 20) to create multi-phase composites. During sintering, cBN can act as a heat-sink (21), lowering the effective local temperature by dissipating heat. Simultaneously, the transition-metal acting as a catalyst (22, 23) could prevent the formation of graphitic  $sp^2$ -phase, thus stabilizing the inherent micro-structure of diamond.

Concurrently, the diamond-to-graphite (24) (or vice-versa (25)) transformation embodies one of the most intriguing phase transitions; thus, understanding and controlling this phase transformation is fundamentally and technologically important (26). Traditionally, the diamond-to-graphite phase transformation (15, 16, 26–33) has been observed through various temperature- pressure driven pathways and exploring new conditions, where diamond-to-graphite phase transformation can be fundamentally different (34–36), and is exciting. Diamond-to-graphite (or vice-versa) phase transformation typically proceeds via extensive bond breaking and rehybridization (26) rather than diffusion-less shear-dominated pathways (35). The crystallographic mismatch between the cubic lattice of  $sp^3$  diamond and the hexagonal lattice of  $sp^2$  graphite makes the diffusion-less, shear-dominated pathway quite improbable, unless the system is subjected to extreme conditions (37), such as mechanical impact.

Here, we report the stabilization of large-scale hard-to-machine, tough diamond-cBN-Co composites from their respective micron-size grain powders using spark plasma sintering. We show that under impact using projectiles at hypersonic speeds (>Mach 8) (closer to hypervelocity where shock-wave effects become prominent), the embedded diamond particles in the composites can transform to graphite in microseconds. Comprehensive experimental analyses and molecular dynamics simulations of the impact events provide insights into diamond's phase stability and atomic-scale transformations that happen under extreme conditions. Our findings could provide a fundamental new understanding of diamond-to-graphite transformation under hypersonic impact, a topic that is becoming increasingly important. Furthermore, it could enable microstructural engineering of

diamond-based multi-phase composites (38–41), with potential applications for extreme condition technologies (37, 42, 43).

## Results

### Synthesis of diamond-cBN-Co composites

We synthesized diamond-cBN-Co composites (equal wt%) using spark plasma sintering (SPS) (**Methods** and **Fig. S1**) at 1400 °C and 90 MPa pressure. The cBN and Co particles were added to prevent the  $sp^2$  bond formation and graphitization of diamond (8). The judicious choice of sintering temperature depends on the fact that Co has a melting point of 1495 °C (1768 K). Other SPS synthesis efforts to obtain diamond-based composites either without using Co or using larger grain sizes of cBN show less success (producing either non-sintered soft disk or more graphitic phases, **Fig. S2** and **S3**). After the optimized sintering attempt, we obtained a dark colored disk (inset of **Fig. 1A**) with a measured density of ~3.32 g/cm<sup>3</sup> (by using the solid cylindrical method). Structurally, X-ray diffraction (XRD) shows diamond D (111) and cBN (111) Bragg peaks dominating (**Fig. 1A** and **Fig. S1J**), their respective most energetically stable facets. We could also observe very small peaks corresponding to graphite (G), suggesting that small amounts of graphite could also form during sintering. We also investigated the orientation of the crystal planes of diamond. The pole figure map shows predominantly (111) faceted diamond grains in random orientation throughout the bulk (**Fig. 1B** and **Fig. S4**). Non-destructive bulk X-ray microscopy (XRM) imaging further exhibits randomly oriented diamond grains (red colors) throughout the bulk of the composite (**Fig. 1C**). As shown through XRM, the diamond particles are found to be less dense and much smaller in size when a diamond-Co disk was attempted to sinter without using cBN (**Fig. S5**), showing the importance of cBN as a matrix (44). The three-phase composite shows  $sp^3$ -hybridized bonding (e.g. C-N and C-B) as evident through X-ray photoelectron spectroscopy (XPS) (**Fig. S6**), that provides a much-improved interfacial thermal stability between cBN and diamond phase (44, 45). The electron probe micro-analysis (EPMA) secondary electron image (SEI) and its wavelength dispersive spectrometry (WDS) elemental maps combining all the elements (**Fig. 1D** and **E**) also shows the surface topography and presence of particles of diamond (red), while the rest of the regions are from uniformly distributed cBN and Co particles, with an obtained wt% of 34.58% (Carbon), 34.54% (BN), and 30.88% (Co). The field emission scanning electron microscopy (FESEM) (**Fig. 1F**) shows particle morphology, further confirming the presence of diamond grains (sizes ~50–100  $\mu$ m). We also show the FESEM image of a single diamond particle (**Fig. 1G**). Its energy dispersive X-ray spectrometry (EDS) elemental map shows that it's a diamond particle embedded with cBN and Co particles (**Fig. 1H**). Raman spectroscopy from these grains shows the characteristic diamond D-band peak at ~1330.9 cm<sup>-1</sup> (**Fig. 1I**) (10). Raman spectroscopy on non-diamond regions show the transverse optical (TO ~1057.08 cm<sup>-1</sup>) and longitudinal optical (LO ~1307.64 cm<sup>-1</sup>) phonon modes (**Fig. 1J**), confirming the

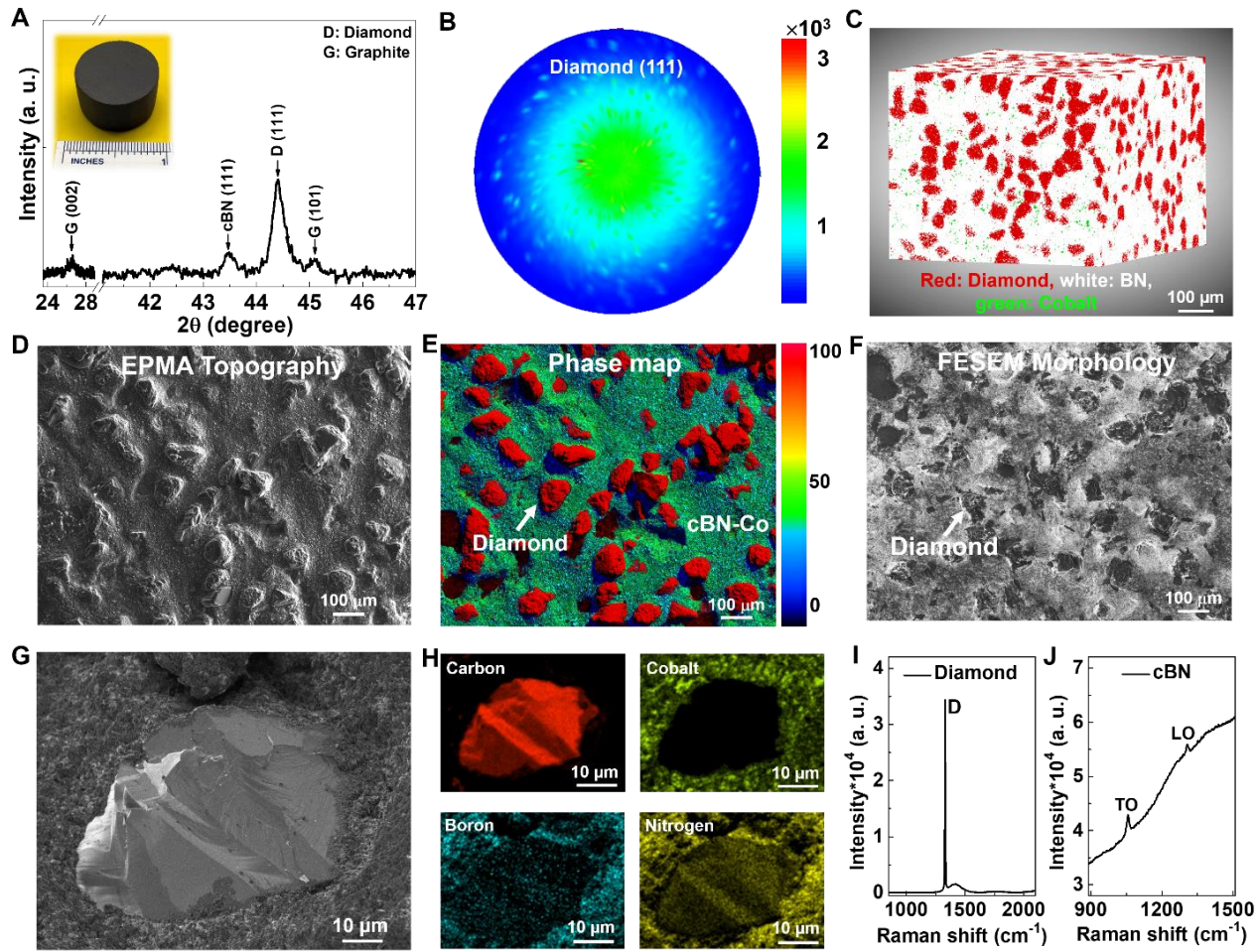


**Figure 1. Characterizations of the diamond-cBN-Co composite.** (A) XRD of the composite shows Bragg peaks of diamond (D), cBN, and graphite (G). Inset shows a spark-plasma sintered black colored disk. (B) XRD pole figure map of (111) diamond peak shows the randomly oriented intensity profiles from the entire sample. (C) Three-dimensional X-ray microscopy imaging shows the diamond particles (red) throughout the composite. (D) EPMA secondary electron image showing the topography, where diamond crystals stand out as high relief grains in the cBN-Co matrix. (E) EMPA WDS phase map shows diamond (red), cBN (green), and Co (light blue). (F) FESEM shows the presence of diamond particles with sizes  $\sim$ 50-100  $\mu\text{m}$  (black). (G and H) A diamond particle is embedded in the cBN-Co matrix. Along with diamond, cBN and Co-rich regions with much smaller particle sizes ( $\sim$ 1-2  $\mu\text{m}$ ) also exist. (I) Raman spectroscopy shows D-band ( $\sim$ 1330.9  $\text{cm}^{-1}$ ) phonon mode from diamond particles. (J) Raman spectroscopy in the non-diamond regions shows transverse optical (TO  $\sim$ 1057.08  $\text{cm}^{-1}$ ) and longitudinal optical (LO  $\sim$ 1307.64  $\text{cm}^{-1}$ ) phonon modes, characteristics of cBN.

presence of cBN particles (21). Functionally, the composite shows Vickers hardness ( $V_H$ )  $\sim 4.30 \pm 2.36$  GPa, elastic modulus  $\sim 33.4$  GPa (**Fig. S7**) and fracture toughness of  $\sim 0.85$  MPa·m $^{1/2}$ . The composite was found to be extremely hard-to-machine (**Fig. S8**) and electrically conducting (resistivity  $\sim 217$  mΩ·cm) at room temperature with a linear V-shape magneto-resistance (due to metallic Co particles embedded in the insulating matrix) (**Fig. S9A**) (46). In addition, the composite shows a ferromagnetic behavior at room temperature (**Fig. S9B**).

## Hypersonic (near-hypervelocity) speed impact testing of the composite

Two diamond-cBN-Co composite samples were subjected to hypersonic speed (near-hypervelocity) impact (**Methods**). In this study, a hypersonic impact is defined as a collision event occurring at a relative speed  $\geq 1700$  m/s. For each test, a cylindrical composite sample was mounted in a custom two-piece 3D-printed axisymmetric target fixture (schematic in **Fig. 2A**). Samples were then tested under two conditions: (1) multiple aluminum 2017-T4 Ø1 mm simultaneously launched distributed particles (SLDPs) at an impact velocity of 2584.7 m/s (Mach 7.5) (**Fig. 2B**), and (2) a single aluminum 2017-T4 Ø4 mm sphere launched at 2900.8 m/s (Mach 8.45) (**Fig. 2E** and **Fig. S10**). High-speed, high-contrast shadowgraphs qualitatively captured the entire impact event, including projectile flight, target impact, ejecta and debris cloud formation and expansion. The SLDP test produced only minor impact surface erosion with no visible cracking or fragmentation (**Fig. 2C, D, and Fig. S11**), demonstrating the composite's high-hardness and superior damage tolerance under distributed loading. In contrast, the Ø4 mm sphere caused macroscopic fracture of the composite sample into several large pieces (**Fig. 2F-H**). In both tests, a fine, powder-like fast-moving front-face ejecta cloud (**Fig. 2C and G**) emanated from the impact face, expanding in the direction opposite to the projectile's motion (i.e. uprange). For the Ø4 mm single-projectile impact, a distinct downrange debris cloud comprising larger fragments was expelled from the target back face (**Fig. 2G and H, and Fig. S12**). In that case, the measured two-dimensional velocities of the leading edges of the front-face ejecta and downrange debris clouds were  $\sim 1122$  m/s and  $\sim 487$  m/s, respectively. Such phenomena, in which the ejecta cloud moves faster than the debris cloud, are relatively common in high-velocity impacts (47, 48). The fragmentation pattern, predominance of fine front-face ejecta, and relatively slower downrange debris are characteristic of impact-driven pulverization in quasi-brittle targets, typically occurring under hypervelocity conditions (49).

To get insights, fully atomistic reactive molecular dynamics (MD) simulations were carried out. An atomic model schematic shows a projectile impacting onto the composite surface at a hypersonic speed (**Fig. 2I**). The projectile was positioned 15 Å uprange from the surface and shot against the target. An overview of the structural and bonding evolution of diamond during and after the projectile impact and the time-dependent evolution of the

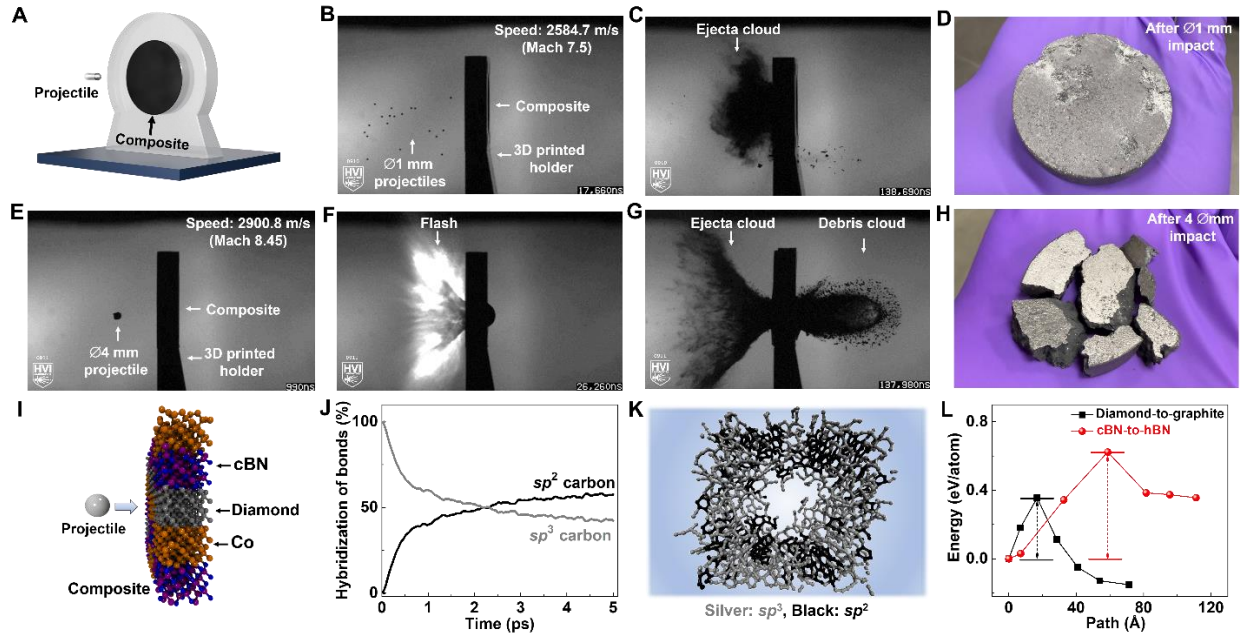


**Figure 2. Hypersonic speed (near-hypervelocity) impact on the composite and its theoretical insights.** (A) Schematic of the impact test where a projectile hit the composite (black disk). The composite is placed onto a 3D printed holder, and spherical aluminum projectiles of  $\varnothing 1$  mm (speed  $\sim 2584.7$  m/s, Mach 7.5) and  $\varnothing 4$  mm (speed  $\sim 2900.8$  m/s, Mach 8.45) are impacted. The impact tests are conducted at ambient conditions. (B and C) High-contrast shadowgraph of the impact event with  $\varnothing 1$  mm projectile. In the lower region, some  $\varnothing 1$  mm projectile missed the impact on the composite, and rather they impacted on the soft holder, creating debris. (D) The survived composite disk after the impact. (E-G) High-contrast shadowgraph of the impact experiment with  $\varnothing 4$  mm projectile, producing flashes, ejecta and debris clouds. (H) The  $\varnothing 4$  mm projectile impact completely shatters the composite disk. In the bottom right of each shadowgraph, the actual time scale of the event is provided. (I) Atomic structural model for the molecular dynamic simulation showing a projectile impacting the composite surface. The projectile was positioned 15 Å above the surface and shot against the target. (J and K) The impact calculation shows a change in  $sp^3$  (decreased) and  $sp^2$  (increased) hybridization bonding of carbon and the formation of a hexagonal graphitic  $sp^2$  carbon structure (black regions) due to impact. (L) The NEB energy barrier calculations for the phase transformation indicating that much higher energy is needed for the cBN-to-hBN phase transformation than diamond-to-graphite.

$sp^2$  and  $sp^3$  hybridizations are shown (Fig. 2J and Fig. S13). We observed a decrease in  $sp^3$  bonds, and an increase in  $sp^2$  bonds immediately after the impact, indicating the graphitization of diamond. Under extreme conditions, the tetrahedral network collapses

into a more disordered, layered configuration. After the impact (**Fig. S13C** and **D**), the surface displays the emergence of interconnected graphitic layers and the formation of internal cavities during structural relaxation. The atomistic view shows the formation of hexagonal rings and graphitic ordering (**Fig. 2K** and **Supplementary text**). Regarding the phase transformation energy required, the Nudged Elastic Band (NEB) calculation shows that  $sp^3$  diamond to  $sp^2$  graphite forms an activation barrier of  $\sim 0.35$  eV/atom (**Fig. 2L**). In comparison,  $sp^3$  cBN to  $sp^2$  hBN transformation exhibits a higher energy barrier of  $\sim 0.62$  eV/atom. These results reveal that both materials are kinetically protected metastable phases, however cBN exhibits a higher resistance (requiring more energy) to hBN phase transformation, compared to diamond-to-graphite.

## Characterizations of the composite after $\varnothing 4$ mm projectile impact test

Post-impact, as the composite disk was completely broken ( $\varnothing 4$  mm projectile impact case); the fragments (**Fig. 2H**) were retrieved from the target tank for characterization. XRD shows a highly intense Graphite G (002) peak along with a much lower intensity D (111) and cBN (111) peaks (**Fig. 3A**). In XRD, the graphite peak is strong, but the formation of the hBN phase was not detectable. For comparison, XRD and Raman spectroscopy of  $\varnothing 1$  mm SLDP impact survived composite, also showing partial graphitization (**Fig. S14**). For the  $\varnothing 4$  mm projectile impact case, pole figure map of the (002) Bragg peak of the fractured composite shows oriented graphite basal planes (**Fig. 3B**), suggesting a certain preferred texture in the diamond transformed graphite. The pole figure map (compared with pristine composite) of the D (111) and G (002), shows some randomness of diamond particles but a more oriented graphite formed after the impact (**Fig. S15**). XRM imaging shows a high volume of graphite (black) throughout the composite and low volumes of diamond having smaller grain sizes (red) (**Fig. 3C**). Hypersonic impacts most likely effectively reduced the Co-cluster (particle) sizes to less than the resolution limit of XRM, thus it is difficult to observe many Co clusters in the XRM image. EPMA SEI shows the topography of the fractured composite sample after the impact (**Fig. 3D**) with small protrusions of diamond particles in the center and a flatter morphology of the graphite flakes. The phase map combined with the WDS elemental maps show carbon surrounded by cBN-Co matrix (**Fig. 3E**). The core-level XPS shows the possible bonding and slight peak shift ( $\sim 0.12$  eV) of the most intense peak in C 1s to lower binding energy, indicating the formation of  $sp^2$  phase (**Fig. S16**). The large-area FESEM morphology shows almost flat layered-sheet-like surface morphology throughout the surface (**Fig. 3F**), very different from the pristine rougher surface with the larger diamond particles. One can clearly see a graphitic layered sheet (almost similar grain size of diamond), and its EDS map further confirming that this graphite (carbon) region is surrounded by cBN (**Fig. 3G** and **H**). Images from several other regions (both from the

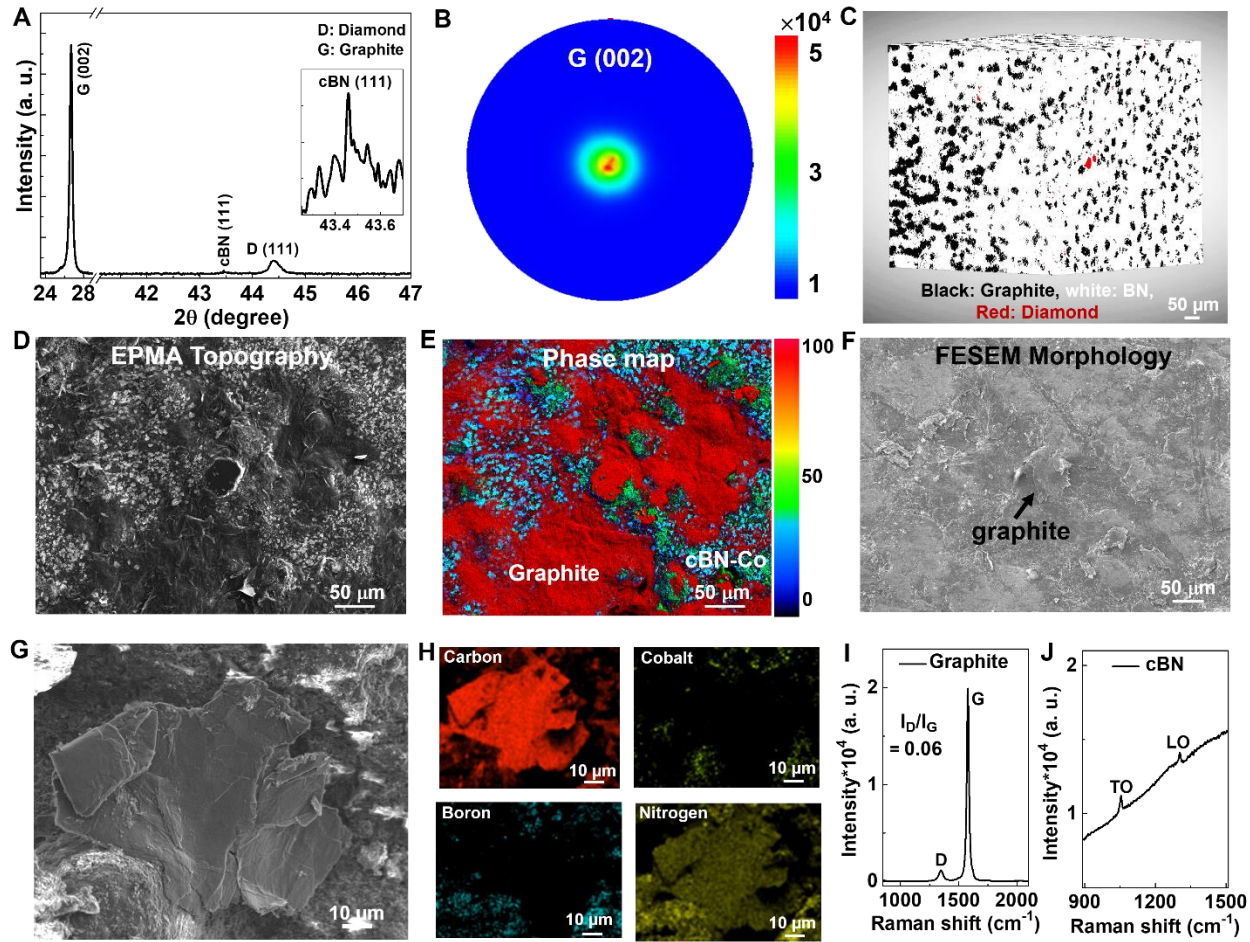


**Figure 3. Characterizations of the composite after the Ø4 mm projectile impact.** (A) XRD shows the highly intense graphite G (002) peak and lower intense diamond (D) and cBN (111) peaks. Inset shows the zoomed-in region of the cBN peak. (B) Pole figure map of G (002) shows oriented graphite throughout the bulk. (C) XRM imaging shows the formation of a high volume of graphitic (black) regions throughout the bulk with a tiny presence of diamond (red). (D) EPMA secondary electron image showing the topography, with a protrusion of smaller diamond-like features in the center, and topography of flatter, larger graphite flakes, surrounded by brighter cBN-Co matrix. (E) Phase map resulting from the combination of WDS element maps shows diamond-graphite (red), cBN (green), and light blue (Co). (F) Large-area FESEM image shows flat surface with layered morphology. (G and H) Image of a graphite layer (almost similar sizes of diamond particle) embedded within the cBN-Co matrix. (I) Raman spectroscopy shows characteristic G-band ( $\sim 1579.07 \text{ cm}^{-1}$ ), and disordered D-band ( $\sim 1345.6 \text{ cm}^{-1}$ ) peaks of graphite. (J) Raman spectroscopy from non-graphitic region shows TO ( $\sim 1053.64 \text{ cm}^{-1}$ ) and LO ( $\sim 1304.06 \text{ cm}^{-1}$ ) phonon modes, characteristics of cBN.

impact surface and the fractured lateral edges) also show formation of layered graphite (**Fig. S17**). The non-carbon regions show the presence of both cBN and Co (**Fig. 3H** and **Fig. S18**). Raman spectroscopy on graphitic layers shows the characteristic G-band peak at  $\sim 1579.70\text{ cm}^{-1}$  along with a defect D-band peak at  $\sim 1345.06\text{ cm}^{-1}$  (**Fig. 3I**). Further in the cBN-Co region, Raman spectroscopy shows TO and LO mode peaks, suggesting the presence of cBN particles (21) (without any signature of hBN peak in the Raman spectra) (**Fig. 3J**). Considering the formation of graphitic layers, the composite now shows more than six-fold increase in electrical conductivity (resistivity  $\sim 36\text{ m}\Omega\text{-cm}$ ), and retains its ferromagnetic behavior at room temperature (**Fig. S19**), however with slightly reduced moments due to the reduction in Co fraction, as seen from the WDS elemental map (**Fig. S20**), due to possible removal of Co during the impact event.

### Atomic-scale insights of the diamond-to-graphite transformation

An atomistic understanding of graphitization of diamond, during impact is important. We investigated the partially graphitized diamond particles to reveal the crystallographic relationship of the transformed graphite layers starting from diamond. In many regions, the FESEM image of diamond particles in the after-impact sample shows the formation of layered sheet-like features around the edges of diamond particles (**Fig. 4A**, **Fig. S21**, and **Fig. S22A**), with the surrounding regions still composed of cBN. EPMA SEI also shows particles that resemble diamond in the original composite in size and shape; however, a closer look at the lower region of the image shows the formation of layered sheet-like features indicating the formation of graphite (**Fig. S22B** and **S22C**). The cathodoluminescence (CL) image shows two distinct emitted intensity profiles from the diamond grain. The intensely red-colored region corresponds to diamond, whereas graphite shows almost no luminescence (**Fig. 4B**). In contrast, the intermediate region showing light-blue towards green indicates the partial transformation of graphite-to-diamond. We also observed the X-ray  $K_{\alpha}$  peak shift from EPMA of carbon for diamond, diamond partially transformed to graphite, and diamond fully transformed graphite, showing distinct peak shifts that are consistent with the graphite EPMA standard reference (**Fig. 4C**). The peak shift reflects the change in the bonding and re-hybridization of carbon during the transformation of diamond to graphite (50).

We performed high-resolution transmission electron microscopy (HRTEM) to capture the diamond-to-graphite phase transformation, which can provide insight into the nature of the phase transformation of diamond particles under impact. The low-magnification bright field (BF) TEM image acquired from cross-sectional focused ion beam (FIB) lamella shows distinct regions of diamond (D), graphite (G) and Co nano-domains, confirmed by the HAADF-STEM image (**Fig. 4D** and **Fig. S23**). The concurrent phase formation of diamond and graphite (the region of interest) was investigated by precession 4D-STEM and diffraction patterns from the respective regions showing [211] and [110] orientations

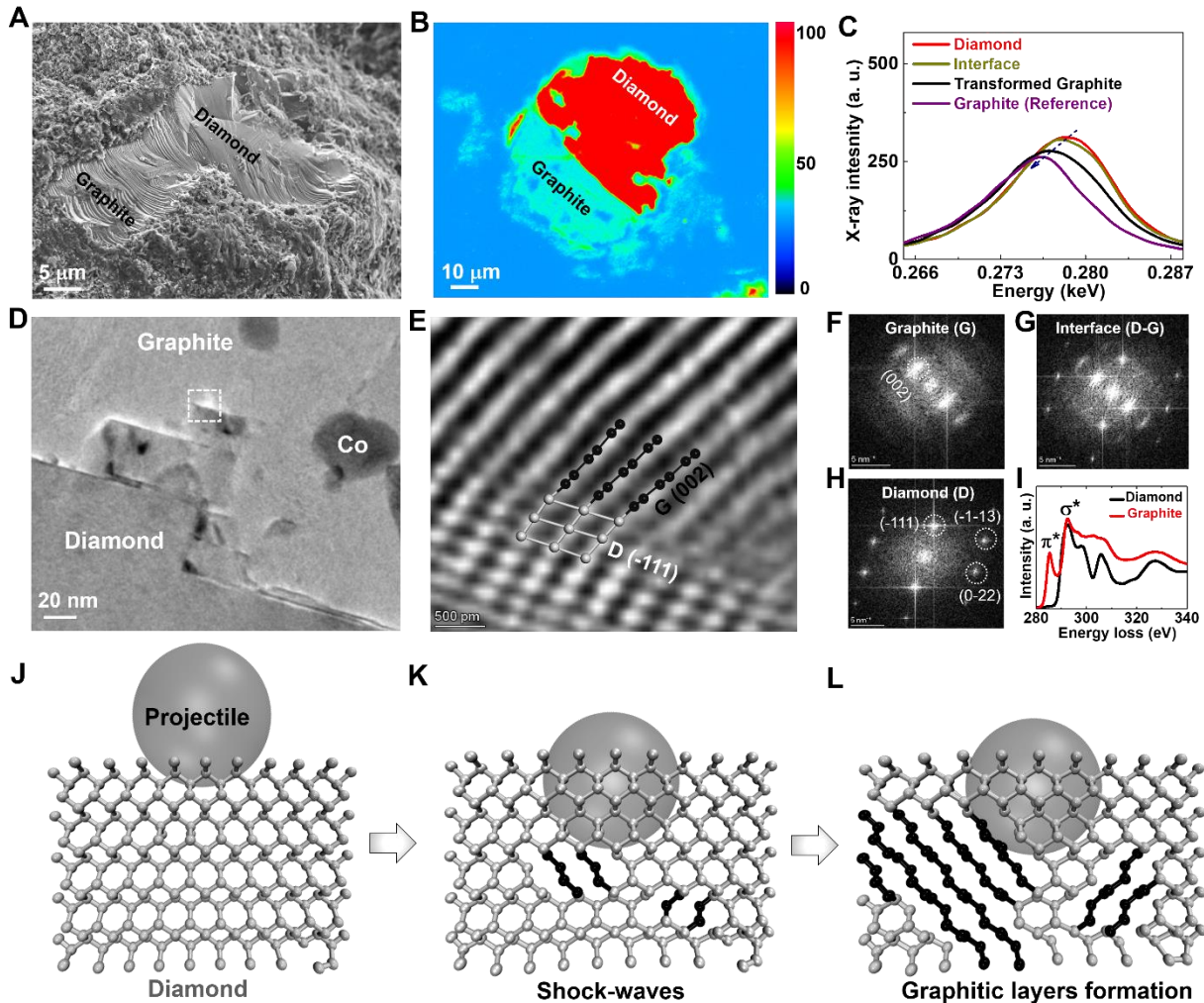


**Fig. 4. Microstructural insights of the diamond-to-graphite transformation.** (A) FESEM showing the layered graphite sheet-like textures within diamond. (B) Cathodoluminescence image shows the emitted intensity from a diamond grain in the visible wavelength range. The red color area represents diamond, the light-blue towards green represents the partially transformed graphite, while the darker light blue is the fully transformed graphite. (C) X-ray  $k_{\alpha}$  peak shifts of carbon from the regions of diamond, partially transformed graphite (near interface), fully transformed graphite, and EPMA standard graphite as a reference. The peak shift attributes the transition from diamond-to-graphite. (D) Bright-field TEM image shows the interface of diamond and graphite. (E) HRTEM image (white box region in 4D) shows the atomic arrangements and interface between diamond and graphite. Atomic structure is shown for clarity with diamond (silver) and graphite (black). (F-H) FFTs patterns from diamond, graphite and the interface showing crystallographic orientation. (I) STEM EELS reveal  $sp^2$  and  $sp^3$  characteristics of diamond and graphite, respectively. (J and K) MD simulations using the ReaxFF show that diamond structure breaks the bonds due to shear (black regions). (L) Fully graphitic layer's formation (black colored for visual representations) due to hypersonic impact, creating diamond-graphite interfaces.

of diamond and graphite lattice (**Fig. S24**). High-magnification HRTEM shows atomic-scale images with one-to-one correspondence between diamond and graphite lattice (**Fig. 4E**). It shows the D (-111) to G (002) atomic orientation relationship at the interface (in the figure we have indicated the structure for clarity). The interlayer spacing of graphite varies across the region due to local bending and it is found to be  $\sim 3.4 \pm 0.1$  Å, the (002) *d*-spacing of bulk graphite phase. The interlayer spacing remains consistent near the diamond-graphite interface, however increasing deviations are observed away from the interface (25). The interlayer *d*-spacing between diamond layers is  $\sim 2.09 \pm 0.05$  Å, suggesting that the lattice is strained (as bulk diamond  $d_{(-111)} = 2.05$  Å).

The corresponding Fast Fourier Transformations (FFTs) from the diamond, graphite and the interface region confirm the crystallographic relation of D (-111) and G (002) planes (**Fig. 4F-H**). The STEM EELS show the characteristic carbon spectra with both  $\pi^*$  (285.4 eV) and  $\sigma^*$  (292.5 eV) peaks of  $sp^2$  bonded graphite, whereas only the  $\sigma^*$  peak of  $sp^3$  bonded diamond (**Fig. 4I**). While graphite forms from the diamond lattice under impact, interestingly, we also observe misorientations between the graphite layers, as confirmed by the diffraction patterns obtained from 4D-STEM of the graphite nano-region with random mis-match angles of 7° and 32° (**Fig. S25**). Rapid impact can induce significant orientation changes between the graphite layers disrupting the natural AB-ordered stacking. Under shock produced during impact, basal planes could rotate or buckle as dislocations and lattice defects proliferate (producing non-coherent interfaces). Further, the impact can also create localized regions of twisting and tilting between adjacent sheets, producing misalignments, as observed here in certain regions. Further, in relatively few locations (compared to the large-scale phase change that has happened to diamond), we also observed localized phase conversion of cBN having  $d_{(111)}$  of  $\sim 2.05$  Å to hBN with  $d_{(002)}$  of  $\sim 3.5 \pm 0.2$  Å (**Fig. S26**), though XRD and FESEM (**Fig. 3A** and **Fig. S18**) showed that predominantly cBN phase was retained after impact. The cubic lattice of Co appeared to remain intact even after the impact (**Fig. S27**).

The impact-induced diamond-to-graphite phase transformation should be an extremely rapid phase change occurring over microseconds, unlike what is normally observed in thermally induced phase change case. During the impact event, the energy absorption could take place in multiple ways. First, fragmentation and formation of large fractured surfaces could dissipate energy via free surface energy creation; this does not appear to be significant, as only a few large target fragments were produced during impact with a single  $\square 4$  mm projectile and the composite sample did not fracture when impacted with  $\square 1$  mm SLDPs. Second, energy absorption could happen via strain-induced massive plastic deformation, which also does not seem to be the case here. Third, significant energy absorption could result from large-scale diamond-to-graphite phase change; we believe this is the primary mechanism occurring in these impact experiments. The fact that the transformation is extremely rapid and mainly non-thermal (although transient temperature spikes could occur locally but this will not be enough to induce the phase

change; interestingly we do not see any phase change in the cobalt), we hypothesize that nonequilibrium pathways driven by shock-waves produced during the impact lead to massive reorganization of the carbon lattice, with diamond transforming into graphite. We investigated the early stage graphitization mechanism using MD simulations with the system modeled using a reactive force-field (ReaxFF). Such a high-speed impact generates intense shock-waves that induce instantaneous pressure spikes followed by rapid release, shear, and localized thermal spikes, concurrently occurring in microseconds (whereas traditional graphitization relies on sustained high temperatures and diffusion processes). This shock generates an intense compressive zone beneath the point of contact, followed by the rapid propagation of elastic waves of shear stresses throughout the diamond lattice (**Fig. 4J-L**). This shear deformation combined with localized thermal spikes forces the  $sp^3$ -bonded tetrahedral framework to collapse into  $sp^2$ -bonded graphitic layers before the system can equilibrate. The highly stressed regions act as nucleation sites for graphitic layers, as the local collapse of the tetrahedral  $sp^3$  framework facilitates the reorganization of carbon atoms into planar  $sp^2$  configurations. As time progresses, the stress field becomes anisotropic, accumulated along the main crystallographic directions favoring structural rearrangement to produce diamond-to-graphite phase transformation.

## Conclusions

In conclusion, we have found a way to stabilize diamond during spark plasma sintering using a unique combination of a matrix material (cBN) and stabilizer (Co), enabling us to create diamond-based hard composites, which are otherwise impossible to produce via sintering. This composite was subjected to hypersonic speed impacts using metal projectiles. During the impact, energy transfer, and fracture event, diamond grains embedded in the composite undergo instantaneous phase transformation to graphite. Atomic-scale structural analyses and atomistic simulations provide insights into the diamond-to-graphite phase transitions and formation of diamond-graphite interfaces during the impact. This impact-induced phase transformation is uniquely important because it probes matter under extreme conditions, revealing fundamental insights into diamond's bonding dynamics, structural instability, and rapid phase kinetics, producing different architectures. Our results provide a unique example of large-scale diamond-to-graphite transition under extreme conditions of impact and shock, never before reported. Finally, our findings would also be important in designing novel diamond-based composite materials, suitable for extreme environments.

## Materials and Methods

### ***Spark plasma sintering of diamond-cubic BN-Co composite***

We performed spark plasma sintering (SPS) by using commercially available yellow color diamond powders (10, 51) (particle size: 50~100  $\mu\text{m}$ , CAS# 7782-40-3, Advalue Technology, Tucson, AZ, USA), gray color cubic BN powders (particle size: 1  $\mu\text{m}$ , SKU: PO6901, MSE Supplies, Tucson, AZ, USA), and black color cobalt powders (particle size: 1.6  $\mu\text{m}$ , 99.5% trace metals basis, CAS# 7440-48-4, BeanTown Chemical, USA). SPS was conducted using an SPS 25-10 system (Thermal Technology LLC, California, USA) at Texas A&M University, USA. A constant uniaxial pressure of 90 MPa was applied, with a heating rate of 50  $^{\circ}\text{C}/\text{min}$ , reaching a maximum temperature of 1400  $^{\circ}\text{C}$ . For SPS, equal wt% diamond, cubic BN and cobalt powders were mixed and ground for 15 min in a mortar pestle. The mixed powder was wrapped in graphite foil and placed inside the graphite die and placed into the SPS chamber under an initial pressure of 5 MPa. Graphite foil serves as a barrier to prevent reactions between the sample and die, while also enhancing thermal distribution and insulation. The chamber was pre-evacuated to  $\sim 2 \times 10^{-5}$  Torr for about 30 minutes, followed by sintering for 60 minutes under ultra-high purity argon gas (5N, ~99.999%). During SPS, a direct current passes through the material, generating the Joule heating process. The temperature during the sintering was monitored using an optical pyrometer (Raytek, Berlin, Germany, model D-13127). After sintering, the pressure was released gradually at  $\sim 5$  MPa/min, while the sample was cooled at  $\sim 100$   $^{\circ}\text{C}/\text{min}$ . For other two composites (Diamond-cBN and diamond-Co), we used same diamond and Co powders and similar SPS conditions, however used larger grain sizes yellow color cBN powders (particle size: 36-54  $\mu\text{m}$ , Batch: 01723C4, MSE Supplies, Tucson, AZ, USA).

### ***Structural characterizations (XRD, Pole figure, XPS, Raman spectroscopy, FESEM)***

X-ray diffraction (XRD) was carried out using a Rigaku SmartLab thin-film diffractometer (Tokyo, Japan), operating at 40 kV and 40 mA with a monochromatic Cu  $\text{K}\alpha$  radiation source ( $\lambda = 1.5406 \text{ \AA}$ ), and a scan rate of 0.05 $^{\circ}/\text{min}$  (short range scan) and 0.2 $^{\circ}/\text{min}$  (wider range scan). For the pole figure map, we used the same XRD instrument in which we performed Chi/phi scans by fixing the detector at the  $2\theta$  positions of the respective phases. We performed X-ray photoelectron spectroscopy (XPS) by using a PHI Quantera SXM scanning X-ray microprobe equipped with a monochromatic Al  $\text{K}\alpha$  source (1486.6 eV). High-resolution core-level elemental spectra were obtained at a pass energy of 26 eV. We used MultiPak V6.1A software to fit the spectra. Raman spectroscopy was conducted using a Renishaw inVia confocal microscope equipped with a 532 nm excitation laser. Surface morphology and the energy dispersive X-ray spectrometry (EDS) mappings were analyzed by field emission scanning electron microscopy (FESEM) using a JEOL JSM IT800 SHL FEG system. For FESEM imaging the energy used was 3 kV whereas for high-resolution EDS maps the energy used was 20 kV.

### ***X-ray microscopy (XRM)***

X-ray microscopy (XRM) images (voxel size ~1.5  $\mu\text{m}$ ) were acquired using a Sigray Eclipse 900 XRM system equipped with an ultrahigh-resolution nanofocus X-ray source operating at 60 kV and a 27-MP large-field-of-view flat-panel detector. Image processing was subsequently performed with 3D Dragonfly software, and a cropped region is presented for clarity. Phase segmentation of diamond and graphite was conducted using the machine learning (ML) algorithm integrated within the software.

### ***Quantitative Electron probe micro-analysis (EPMA)***

Quantitative EPMA data acquisition was carried out on a Jeol JXA 8530F Hyperprobe, equipped with a Schottky field emission gun and five Wavelength Dispersive Spectrometers (WDS). Both samples (before and after impact) were coated with amorphous carbon to eliminate the eventual discharge, assuring ground conductivity. The carbon film thickness was 25 nm, similar to the carbon film deposited on the reference standards used in the quantitative analysis (diamond, BN, and Cobalt metal). Analytical conditions employed for analysis were an accelerating voltage of 15 kV, beam current of 50 nA, and spot beam size (~350 nm diameter). The PAP method was employed for quantification (52). The experimental parameter details are presented in **Table S1**. Detector conditions for each element are shown in **Table S2**. Quantitative Wavelength Dispersive Spectrometry (WDS) elemental maps were acquired at 15 kV accelerating voltage and 50 nA beam current, using stage mode with 200 ms dwell time. Different elements were mapped by recording the relative intensity of their characteristic X-ray line (**Table S1**). The same standards used for quantitative analysis were employed for the quantification of element maps. Deadtime correction was applied for each element map. The map resolution is  $550 \times 470$  pixels, with 1 pixel = 1.2  $\mu\text{m}$ , or the size  $660 \mu\text{m} \times 564 \mu\text{m}$ . WDS qualitative analysis (WDS scans) employed the same accelerating voltage and beam current as in the quantitative analysis. The scan interval was between 0.264 to 0.290 keV, at a step of 0.000066 keV. The peaks were smoothed using the Savitzky-Golay method ('auto smoothing' mode).

### ***Electrical transport and magnetization***

The temperature-dependent AC resistivity between 2K-300 K was measured using the Quantum Design Physical Property Measurement System (PPMS) employing the standard four-point probe method with silver point contacts. A constant current of 2 mA was applied, and the corresponding voltage was recorded while the temperature was swept at a rate of 1 K/min. The magnetoresistance (MR) was performed with the electrical current applied in-plane (*ab*-plane) and the magnetic field applied oriented within the *ab*-plane over a field range of -5 to 5 T.

Field-dependent magnetization (M-H) was measured at 300 K using the DC measurement mode of a Quantum Design Magnetic Property Measurement System

(MPMS 3) equipped with a 7 T superconducting magnet. The sample was mounted in a standard plastic straw holder, and the M-H loops were collected between -5 and 5 T at a field sweep rate of 200 Oe/sec using the auto-centering option.

### ***Vickers hardness testing***

Vickers microhardness measurements were performed using a LECO LM310 hardness tester. Prior to testing, a flat region ( $500 \mu\text{m} \times 500 \mu\text{m}$ ) suitable for indentation was prepared using a plasma-focused ion beam (FIB). The FIB milling was used to remove the as-received surface roughness and generate a smooth, planar area large enough to accommodate multiple indents without interaction. Indentations were carried out under a Vickers diamond indenter with 0.5 kgf (kilogram-force), using the standard loading-unloading sequence of the instrument. For each condition, five indents were placed within the FIB-flattened region, ensuring sufficient spacing to avoid overlapping of plastic zones. The two diagonals of each indent were measured using the built-in optical microscope of the LM310, and the Vickers hardness was calculated from the average diagonal length according to the standard Vickers relation. The fracture toughness was measured from Vickers indentation cracks by using the Anstis equation (53, 54)  $K_{IC} = 0.16\left(\frac{H}{E}\right)^{1/2} \frac{P}{c^{3/2}}$ , where  $E$  is the elastic modulus,  $H$  is the hardness,  $P$  is the applied load, and  $c$  is the distance from the indent center to the crack tip.

### ***Compressive testing with digital image correlation (DIC)***

Uniaxial compression tests were performed using an Instron universal testing machine equipped with a calibrated load cell. Specimens were aligned between two flat, polished platens and loaded under displacement control at a constant cross-head rate chosen to ensure quasi-static conditions. The front surface of each specimen was lightly sprayed with a white matte base coat, followed by a fine black speckle pattern to enable digital image correlation (DIC). During testing, images of the speckled surface were acquired using a CCD camera equipped with a macro-lens, synchronized with the load-displacement data acquisition. DIC analysis was carried out using Ncorr, an open source 2D DIC MATLAB program. For each frame, the axial strain component  $\varepsilon_{yy}$  was computed from the full-field displacement map using a subset size and step chosen to balance spatial resolution and noise. A rectangular region of interest (ROI) was defined in the central gauge section of the specimen, excluding the edges and the indenter/contact zones. The average axial strain at each load step was then obtained as the arithmetic mean of all valid DIC subsets within the ROI,

$$\bar{\varepsilon}_{yy} = \frac{1}{N} \sum_{i=1}^N \varepsilon_{yy,i},$$

where  $N$  is the number of subsets in ROI. The apparent elastic modulus was determined from the slope of the nominal stress  $-\varepsilon_{yy}$  curve in the initial linear regime of loading.

### ***Elastic modulus***

Compressive loading tests were performed in conjunction with DIC to obtain full-field displacement and strain maps during loading. For each load step, the axial strain component  $\varepsilon_{yy}$  was exported over a rectangular region of interest (ROI) centered in the gauge section, excluding the sample edges and the indenter/contact zone. Using this procedure, an average axial strain of  $\varepsilon_{yy} \approx 2 \times 10^{-4}$  was obtained at the maximum load used for elastic calibration. Combining this strain with the nominal stress from the load cell gives an apparent elastic modulus. Because the actual contact area at the top surface is reduced by surface imperfections and non-planarity, this value is considered a lower bound for the composite.

### ***Hypersonic speed (near-hypervelocity) impact test***

The impact experiment was performed at Texas A&M University (TAMU) Hypervelocity Impact Laboratory (HVIL) using a two-stage light-gas gun (2SLGG) and aeroballistic range. The gun is capable of launching large numbers of 0.1-2.0 mm variable-shaped particle clusters (“simultaneously launched distributed particles” or SLDPs) or wide variety of 1.6-10 mm diameter single projectiles of various geometries (spherical, cylindrical, ogival, etc.) at velocities of 2-8 km/s. The 2SLGG is capable of accelerating projectiles at hypervelocity (typically  $\geq 3$  km/s) by compressing a light working gas (e.g., hydrogen) to high pressure using a gunpowder charge and a consumable polymer piston. In the first stage, the combustion gases from the gunpowder ignition propels the polymer piston down an enclosed pressurized tube (i.e., “pump tube”) containing the light working gas. Once the light gas is compressed to a critical pressure (typically 45-63 MPa), a diaphragm at the downrange end of the pump tube ruptures, releasing the high-pressure gas that accelerates the projectile package down a launch tube to the desired velocity. The light gas compression in the pump tube constitutes the second and final stage necessary to accelerate the projectile. A more complete overview of the TAMU HVIL 2SLGG facility, including the operational details and diagnostic capabilities, is provided (**Fig. S28**) (55).

The cylindrical composite disks ( $\varnothing 40$  mm, and  $\sim 7.4$  mm and  $\sim 6.6$  mm thick, respectively) were mounted in custom two-piece 3D-printed (polylactide) axisymmetric target fixtures. The fixture contained a central circular aperture such that the impact- and back-faces of the sample were clamped between the two pieces using four evenly spaced fasteners. This target assembly was secured to a mounting fixture in the target tank, with the sample centered about the projectile flight axis. The disks were then impacted with several  $\varnothing 1$  mm (total mass of 0.049 g) at 2584.7 m/s and a single  $\varnothing 4$  mm 2017-T4 aluminum sphere

(mass of 0.091 g) at 2900.8 m/s. The projectile's velocity was measured using a dual-laser-curtain velocimetry system, with an accuracy of  $\pm 2$  m/s. A total of 128 shadowgraphs of each impact event were recorded using a Shimadzu HPV-X2 operating at 751,880 frames per second with an interframe exposure time of 200 ns. The open-source Tracker motion-tracking software (version 6.3.2) was used to determine the 2D velocity of the expanding leading edges of ejecta and debris clouds from the high-speed shadowgraphs.

### ***High-resolution transmission electron microscopy (HRTEM)***

A double aberration corrected Themis Z (ThermoFisher Scientific) TEM equipped with a Super-X energy dispersive X-ray detector (EDX) and a Gatan GIF Continuum 970 HighRes camera was used for atomic scale characterization at an accelerating voltage of 300 kV. A cross sectional TEM lamella was prepared by focused ion beam using Helios dual beam (ThermoFisher Scientific) FIB. High resolution imaging was performed in both transmission (TEM) and scanning (STEM) mode. STEM and TEM images were acquired using a high-angle annular dark field (HAADF) and annular bright field (ABF) detector and Ceta 16 M camera. Electron energy loss spectra (EELS) in STEM were collected with 2.5 mm aperture at an energy dispersion of 0.1 eV per channel and 1.1 eV energy resolution. 4D-STEM measurements for phase and orientation mapping were carried out using NanoMegas ASTAR system with a precession electron diffraction (PED). The microscope operated in micro-probe STEM mode with a 0.5 mrad convergence angle and a camera length of 245 mm. The precession angle was set to 0.6° and diffraction patterns were collected using a pixelated Dectris Quadro Detector.

## **Theoretical calculations**

### ***Energy barrier calculations***

The energy interconversion barriers were estimated using Nudged Elastic Band (NEB) simulations (56). We employed the Self-Consistent Charge Density Functional Tight-Binding (SCC-DFTB) method, as implemented in the DFTB+ code (57), using the Slater-Koster matsci-0-3 parameter set. Diffusion barriers were computed using the NEB method as implemented in the Atomic Simulation Environment (ASE) framework (58). The diamond (or cBN) and graphite (or hBN) structures were used as initial and final configurations, respectively, with five interpolated images generated along the minimum energy pathway (MEP). The Improved Dimer Projection Path (IDPP) algorithm (59) was applied to refine the initial interpolation, ensuring a more accurate representation of the transition pathway and saddle-point region. Geometry optimizations for all images were carried out using the BFGS algorithm until the maximum residual force on any atom was below 0.05 eV/Å, yielding well-converged transition-state configurations.

### ***Molecular dynamics (MD) simulations using a reactive force-field (ReaxFF)***

To investigate the insights about the projectile impacting on a diamond surface, fully atomistic reactive molecular dynamics (MD) simulations were carried out using the LAMMPS code (60). The systems were modeled using the reactive force field ReaxFF (61), which accurately describes bond formation and dissociation, bond-order variations, and charge redistribution. Charge equilibration was performed at every integration step using the qeq/reaxff algorithm with a convergence tolerance of  $10^{-6}$ , ensuring consistency in energy, forces, and atomic charges, even under highly nonlinear conditions typical of hypersonic regimes.

The simulation cell was a cubic box with dimensions of 200 Å, with periodic boundary conditions along all directions. The diamond target was created from a  $10 \times 10 \times 5$  supercell, containing 4000 atoms. The idealized projectile center of mass was positioned 25 Å above the target surface and assigned an initial velocity of 29 Å/ps along the z-direction, corresponding to approximately Mach 8.45. Its mass was set equal to that of the substrate to maximize momentum transfer and impact intensity.

The equations of motion were integrated using the velocity-Verlet algorithm (62) with a timestep of  $1.0 \times 10^{-4}$  ps during thermal equilibration and  $5.0 \times 10^{-5}$  ps during the impact event. This choice ensured numerical stability in the presence of large forces and rapid charge redistribution inherent to the ReaxFF potential. To prevent computational errors in bond detection under extreme compression, the ReaxFF implementation employed extended safety buffers, thereby enhancing numerical robustness without altering the system's physical behavior.

The simulation protocol began with an energy minimization using a convergence criterion of  $10^{-6}$  for both energy and forces to remove any residual atomic overlaps. Subsequently, a 10 ps equilibration MD run was performed in an NVT ensemble, maintaining the system at 300 K using a Nosé-Hoover thermostat (63, 64). After equilibration, the simulation was changed to an NVE ensemble to ensure energy conservation during the impact event. The projectile interacted with the targets via a purely repulsive Weeks-Chandler-Andersen (WCA) potential (65, 66), designed to eliminate any attractive components that could lead to artificial adhesion or unintended chemical reactions. The WCA parameters were set to  $\sigma = 10$  Å and  $\epsilon = 5$  eV, with a truncation at  $r_c = 2^{1/6}\sigma$  and an energy shift such that  $V(r_c) = 0$ , ensuring a smooth potential cutoff.

## Acknowledgements

P. M. A. acknowledges the support from Air Force Office of Scientific Research (AFOSR) under award number FA9550-24-1-0301. The authors gratefully acknowledge the support of the Texas A&M University (TAMU) Hypervelocity Impact Laboratory (HVIL) for enabling the impact experiments. R. S. and C. K. are grateful to the Karlsruhe Nano Micro Facility (KNMFi) at KIT for providing TEM facilities. L. Z. D. acknowledges the funding support provided by the Robert A. Welch Foundation (00730-5021-H0452-B0001-G0512489). S. K., C. W. C. and L. Z. D acknowledges support from the U.S. Air Force Office of Scientific Research Grants FA9550-15-1-0236 and FA9550-20-1-0068; the T. L. L. Temple Foundation; the John J and Rebecca Moores Endowment; and the State of Texas through the Texas Center for Superconductivity at the University of Houston. T. F., L. L., Y. Z., and S. Y. acknowledges financial support from the Natural Sciences and Engineering Research Council of Canada (NSERC) and the Canada Foundation for Innovation (CFI). G. C. acknowledges the use of the EPMA facility at the Department of Earth Science, Rice University. Marcelo L. Pereira Junior acknowledges financial support from the Federal District Research Support Foundation (FAPDF) under grant 00193-00001807/2023-16, from the National Council for Scientific and Technological Development (CNPq) under grants 444921/2024-9 and 308222/2025-3, and from the Coordination for the Improvement of Higher Education Personnel (CAPES) under grant 88887.005164/2024-00. Raphael B. de Oliveira thanks CNPq for support under processes 151043/2024-8 and 200257/2025-0. Guilherme S. L. Fabris acknowledges support from the São Paulo Research Foundation (FAPESP) through fellowship 2024/03413-9. Douglas S. Galvão acknowledges support from FAPESP under grant 2025/27044-5 and from the Research, Innovation, and Dissemination Centers (CEPID) program under grant 2013/08293-7. It is also acknowledged for support from INEO/CNPq and FAPESP grant 2025/27044-5. We also thank the Coaraci Supercomputer Center for providing computational resources under process 2019/17874-0. A. B. thanks Texas A&M user facility and A. Bandyopadhyay for the SPS. P. M. A. would like to thank Ramon Torrecillas for technical help. X-ray facilities managed by the Shared Equipment Authority of Rice University.

## **AUTHOR DECLARATIONS**

### **Competing interests**

The authors declare that they have no known competing financial interests.

### **Author contributions**

A. B. and P. M. A. conceptualized the work. A. B., J. M., S. C., and J. L. performed the materials synthesis and characterizations. A. M., A. B., P. M. A., and T. L. Jr. performed the impact tests. R. S. and C. K. performed the HAADF-STEM. S. Y., L. L., Y. Z., and T. F. performed the nanoindentation. M. L. P. J., R. P. O., G. S. L. F., and D. S. G. performed the theoretical calculations. G. C. performed the EPMA. S. K., C. W. C., and L. D. performed the electrical transport measurements. A. B., R. V., and P. M. A. analyzed the data. A. B. and P. M. A. wrote the paper with the help of all the authors. All the authors discussed the results and contributed to the manuscript preparation.

### **Data availability**

All data are available in the Main text, Methods or in the Supplementary Information. Additional data related to this paper may be requested from the corresponding authors upon reasonable request.

**Supplementary Materials for**  
**Diamond-to-graphite transformation under hypersonic impact**

Abhijit Biswas *et al.*,

\*Corresponding authors: **abhijit.biswas@rice.edu; ajayan@rice.edu**  
A. Mote, R. Sahu, and M. L. Pereira Junior contributed equally to this work.

**It includes:**

Fig. **S1** to **S28**  
Tables **S1** and **S2**  
Supplementary Text

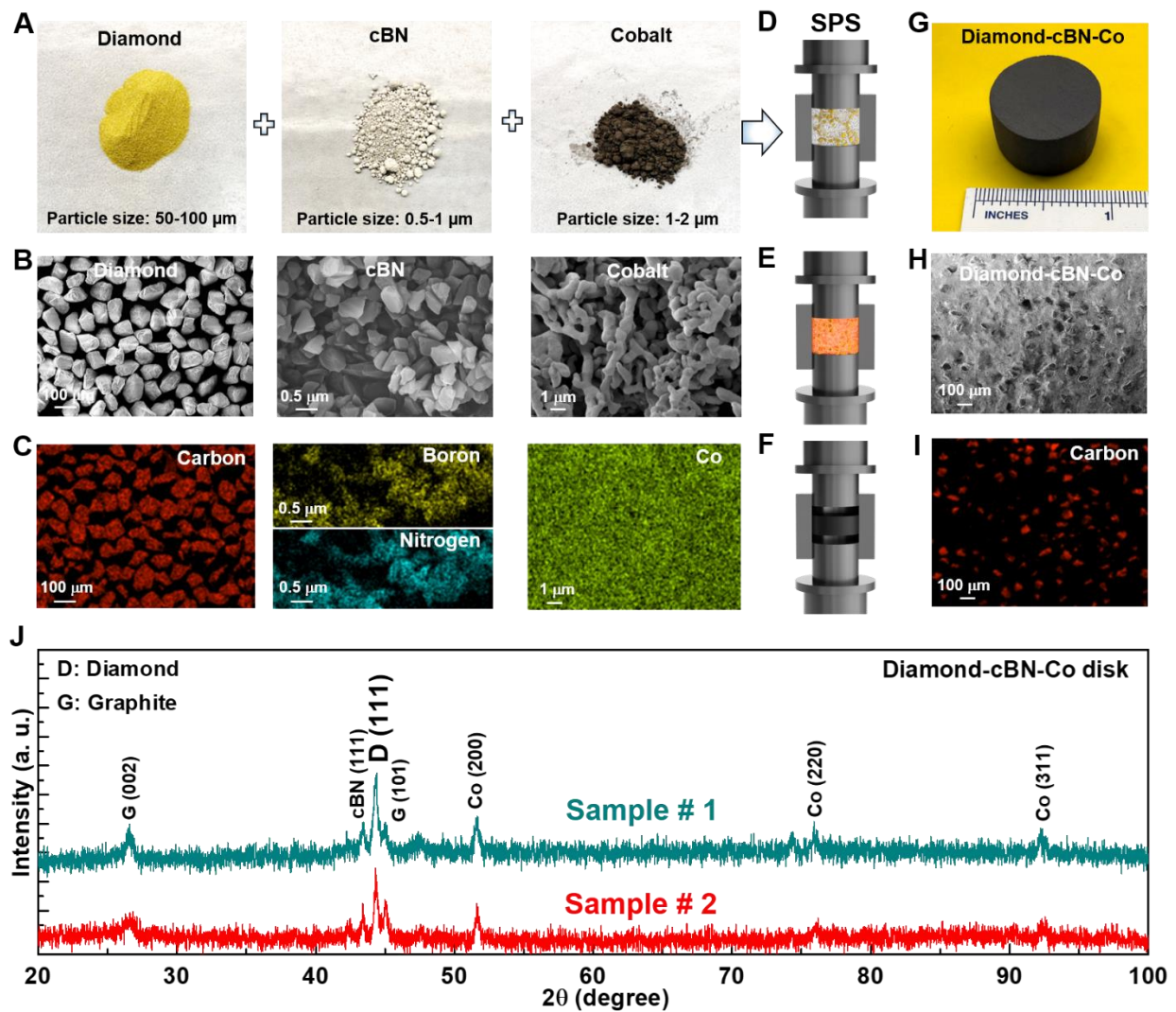


**Fig. S1. Synthesis of diamond-cBN-Co composite.** (A) Commercially available diamond, cubic boron nitride (cBN) and cobalt (Co) powders with different particle sizes are mixed homogeneously in a mortar pestle for 15 min before placing them into the SPS chamber. Diamond powder is yellow due to the presence of nitrogen (51), causing the diamond to reflect yellow light. (B and C) Corresponding FESEM images and EDS elemental mapping show different grain sized particles. (D-F) Schematic of the SPS process which was performed at 1400 °C, 90 MPa pressure for 1 hr in high purity 5N Argon atmosphere. (G-I) SPS produced black colored disk, and its FESEM surface morphology and EDS elemental mapping of carbon showing the presence of diamond particles throughout the sample. (J) Wider 2θ range XRD scans of two different samples sintered at the same conditions.

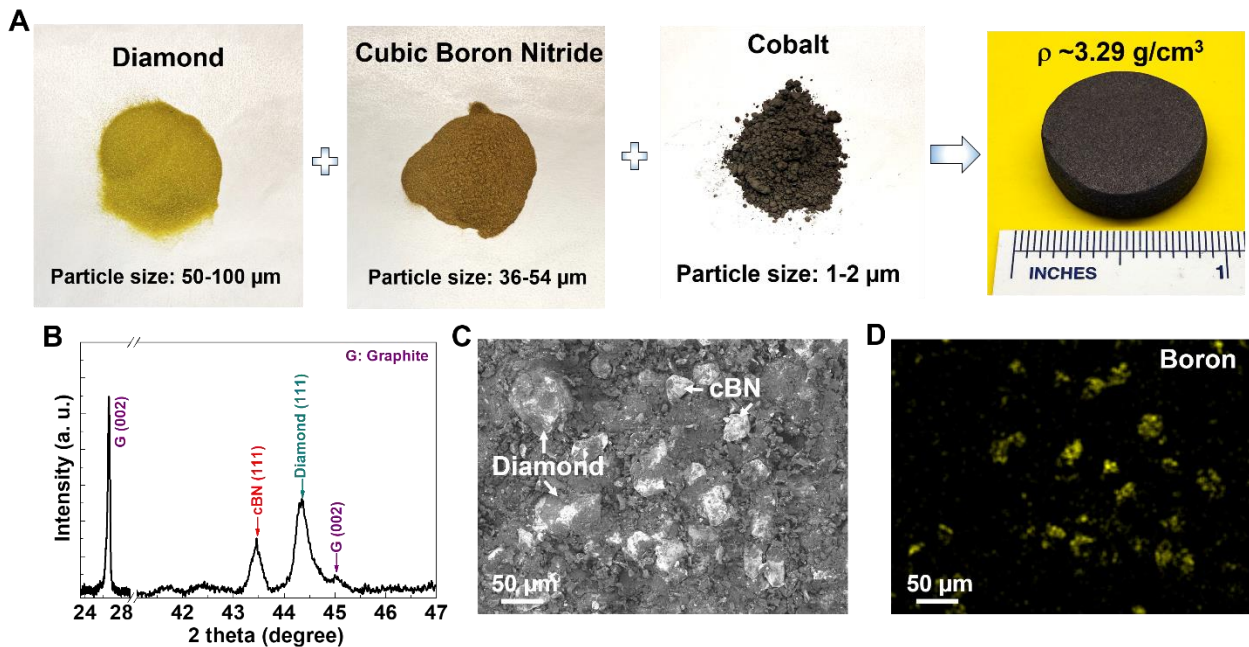


**Fig. S2. Synthesis attempt of diamond-cBN-Co composites by using larger grain sizes of cBN particles. (A)** Respective diamond, cBN and cobalt powders and sintered disk. The larger grain sizes cBN powder is yellowish due to defects. **(B)** Corresponding XRD pattern showing the intense graphite (002) peak. **(C)** FESEM surface morphology shows the presence of the diamond and cBN particles. **(D)** EDS elemental map of boron confirms the presence of cBN particles. The composite was sintered at the same SPS conditions of 1400 °C, 90 MPa pressure, for 1 hr.

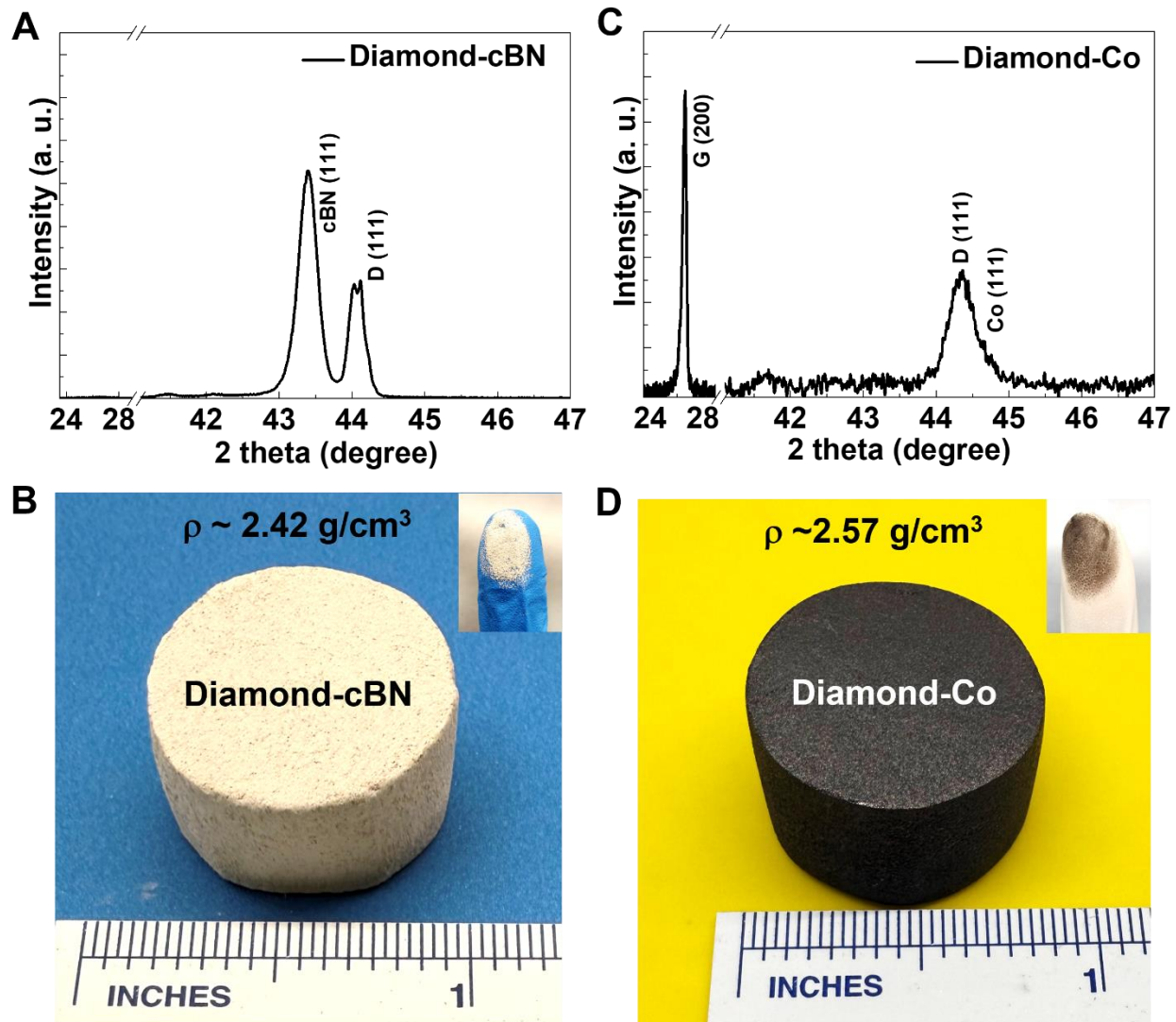


**Fig. S3. Synthesis attempts of the diamond-based composite using diamond-cBN or diamond-Co. (A and B) Synthesis attempt of diamond-cBN composite (without Co) producing an ultra-soft disk (almost non-sintered) which can be easily broken (rubbed) by pressing with finger tips (upper right inset of B). (C and D) Synthesis of diamond-Co composite (without cBN) which is comparatively harder, however shows the presence of a more intense graphitic peak than diamond. Again, the sintering conditions are the same of 1400 °C, 90 MPa pressure, for 1hr, as used for the main diamond-cBN-Co composite.**

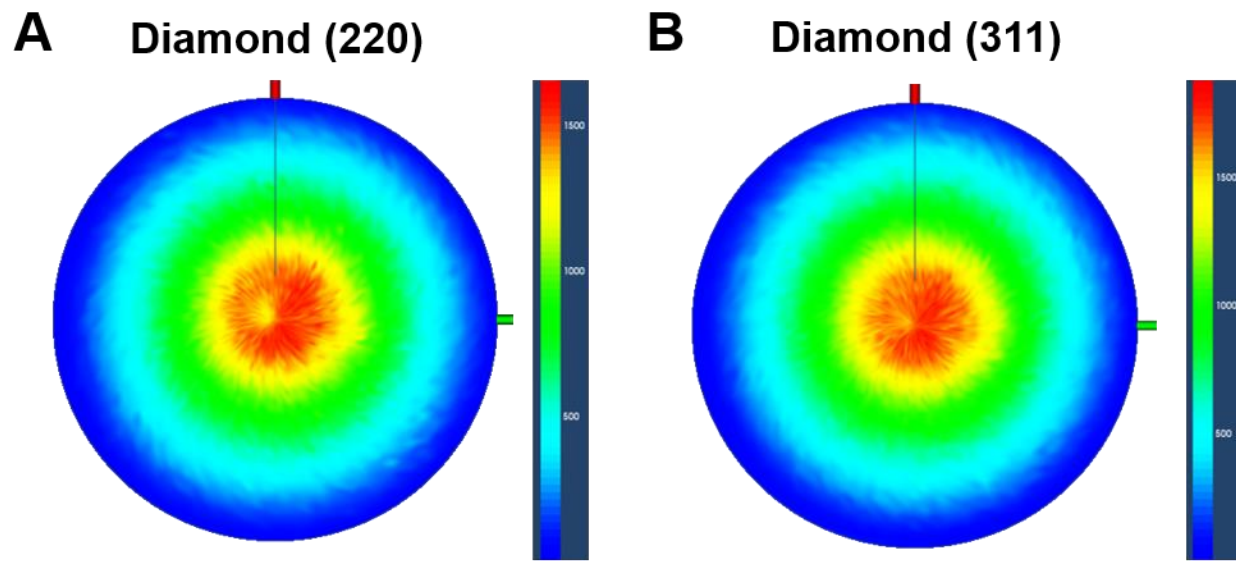


**Fig. S4. Pole figure mapping of the composites.** (A and B) XRD pole figure map of the (220) and (311) Bragg peaks of diamond show no grain-like features distributed throughout the sample (as like the (111) peak pole figure case, main **Fig. 1B**), possibly having very small numbers of facets with relatively lower intensity.

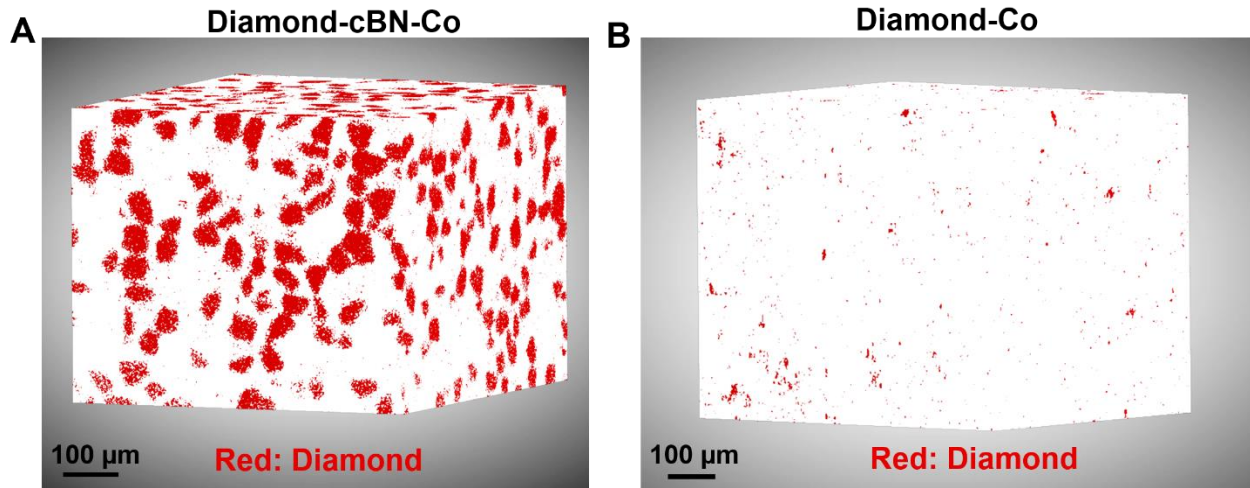


**Fig. S5. X-ray microscopy imaging of the composite.** (A) X-ray microscopy imaging of diamond particles (red) in the three-phase diamond-cBN-Co composite. (B) In comparison, X-ray microscopy imaging of the diamond particles (red) in the diamond-Co composite (without cBN), showing smaller particle sizes with a lower volume of diamond. Here we kept non-diamond regions white for better visualization of diamonds. This shows that addition of cBN as a matrix helps in stabilizing diamond.

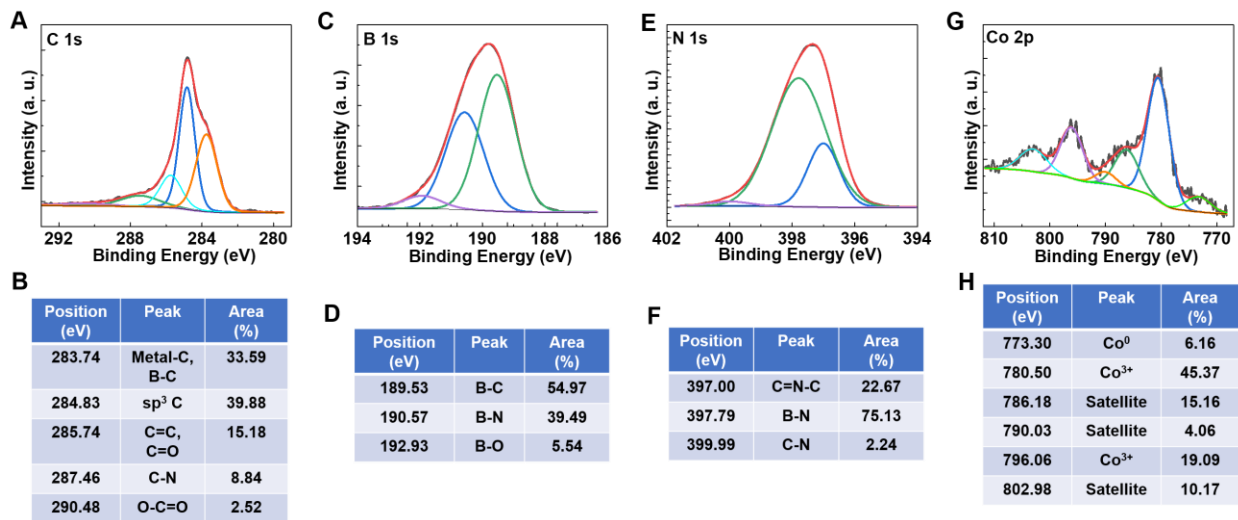


**Fig. S6. XPS of the sintered pristine three-phase diamond-cBN-Co disk.** Core-level XPS scans and its fitting show various possible bonding for (A and B) C 1s, (C and D) B 1s, (E and F) N 1s, and (G and H) Co 2p.

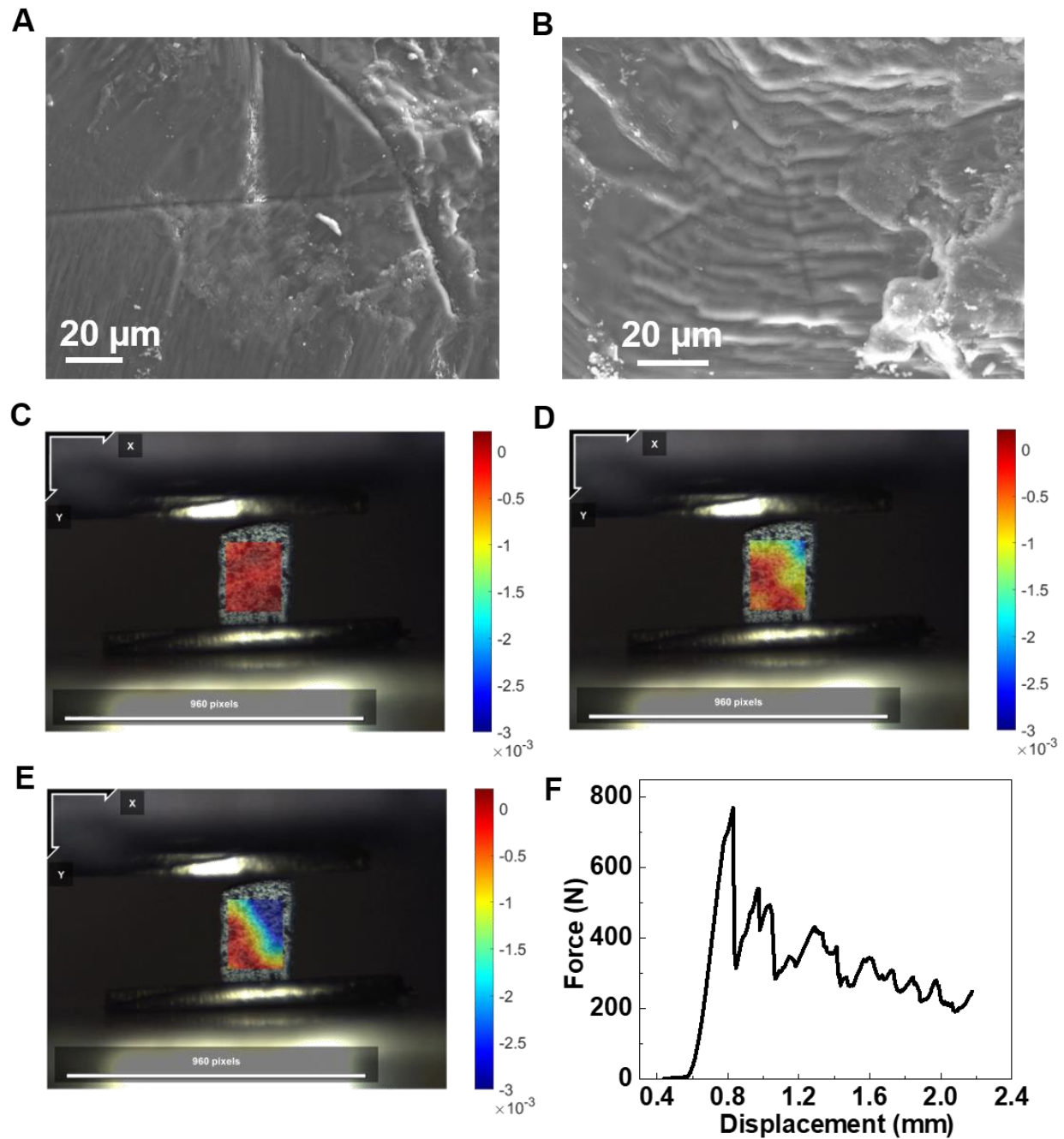


**Fig. S7. Mechanical characterizations of the diamond-cBN-Co composite. (A and B)** SEM micrograph showing the indented regions at various regions with 5N load. **(C-E)** Compressive testing with digital image correlation (DIC) in which the images of the speckled surface were acquired using a CCD camera equipped with a macro-lens and synchronized with the load-displacement data acquisition. **(F)** Compression curve in conjunction with digital image correlation (DIC) to obtain full-field displacement and strain maps during loading.

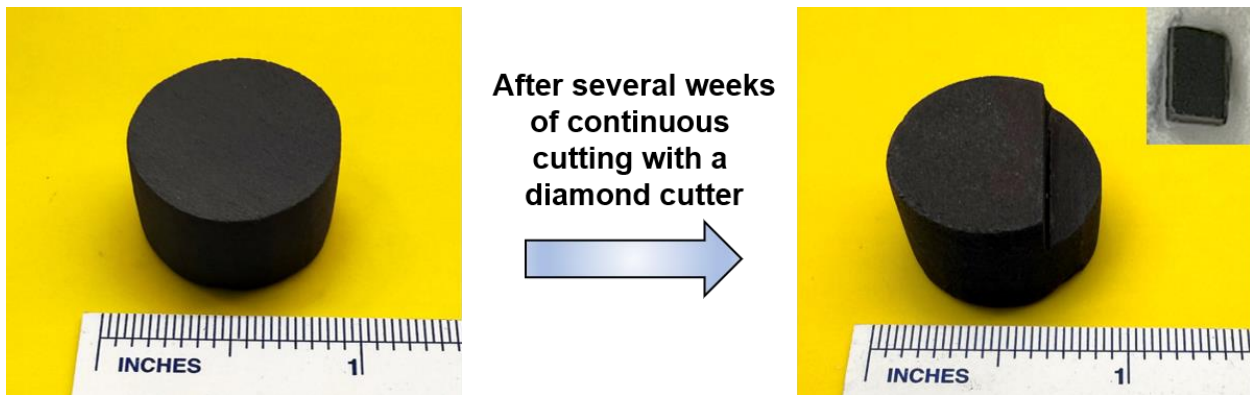


**Fig. S8. Machining of the diamond-cBN-Co composite.** A low-speed diamond saw (Model 650, South Bay Technology Inc.) with dimensions of 13" W  $\times$  9" H  $\times$  13" D and a maximum wheel speed of 300 rpm was used to cut the composite disk. A rectangular sample piece of about 3 $\times$ 2 mm<sup>2</sup> (inset) was obtained after continuous cutting for eight days. During cutting, the diamond wheel operated at its maximum speed (300 rpm) while fully submerged and rotating through a bath of isopropanol to minimize friction. The pieces were subsequently used for mechanical, electrical, and magnetization measurements.

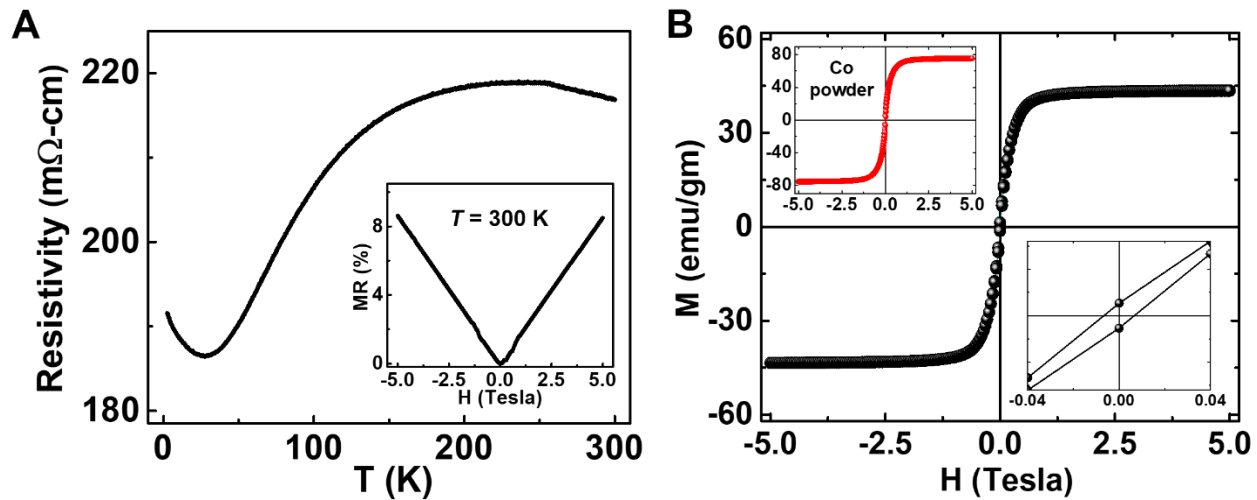


**Fig. S9. Electrical transport and magnetic properties of the diamond-cBN-Co composite.** (A) Composite is electrically conducting with room temperature resistivity of  $\sim 217$  mΩ·cm. Inset shows the V-shape linear field-dependent magnetoresistance. (B) It shows ferromagnetic behavior at room temperature with a hysteretic M-H loop with a low coercivity of  $\sim 656$  Oe, shown in lower-right inset. Upper-left inset shows the ferromagnetic loop of pure cobalt (Co) powder.

Projectile material type	Specific projectile material	Projectile diameter (mm)	Sabot (mm)	L/D ratio	Projectile mass (g)	Projectile package mass (g)	Projectile shape	Projectile speed (m/s)	Projectile KE (kJ)	Target temperature (°C)	Room temperature (°C)	Room humidity (%)
Aluminum (Al)	2017-T4 Aluminum	BS-1.00	6	1	0.049	2.075	Sphere (S)	2584.7 (Mach 7.5)	0.16	21.2	21.1	57
Aluminum (Al)	2017-T4 Aluminum	4	4	1	0.091	2.136	Sphere (S)	2900.8 (Mach 8.45)	0.38	21.2	21.1	57

**Fig. S10. Parameters used for the impact test.** Impact tests with several  $\varnothing 1$  mm (upper panel) and with a  $\varnothing 4$  mm (lower panel) aluminum metal balls as projectiles.

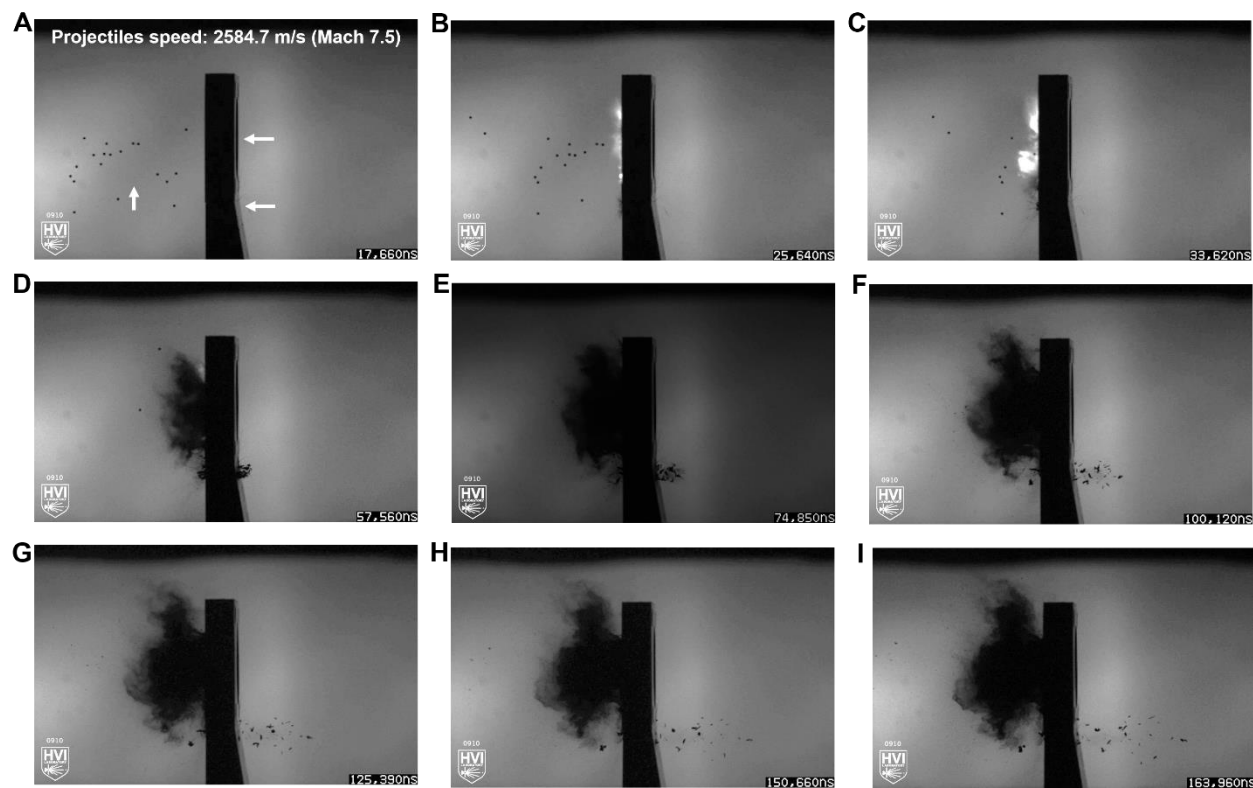


**Fig. S11. Shadowgraphs of the impact test with  $\varnothing 1$  mm projectile (speed 2584.7 m/s, Mach 7.5). (A-I)** High-contrast shadowgraphs of the impact event at different time-scales with several  $\varnothing 1$  mm aluminum spherical projectile.

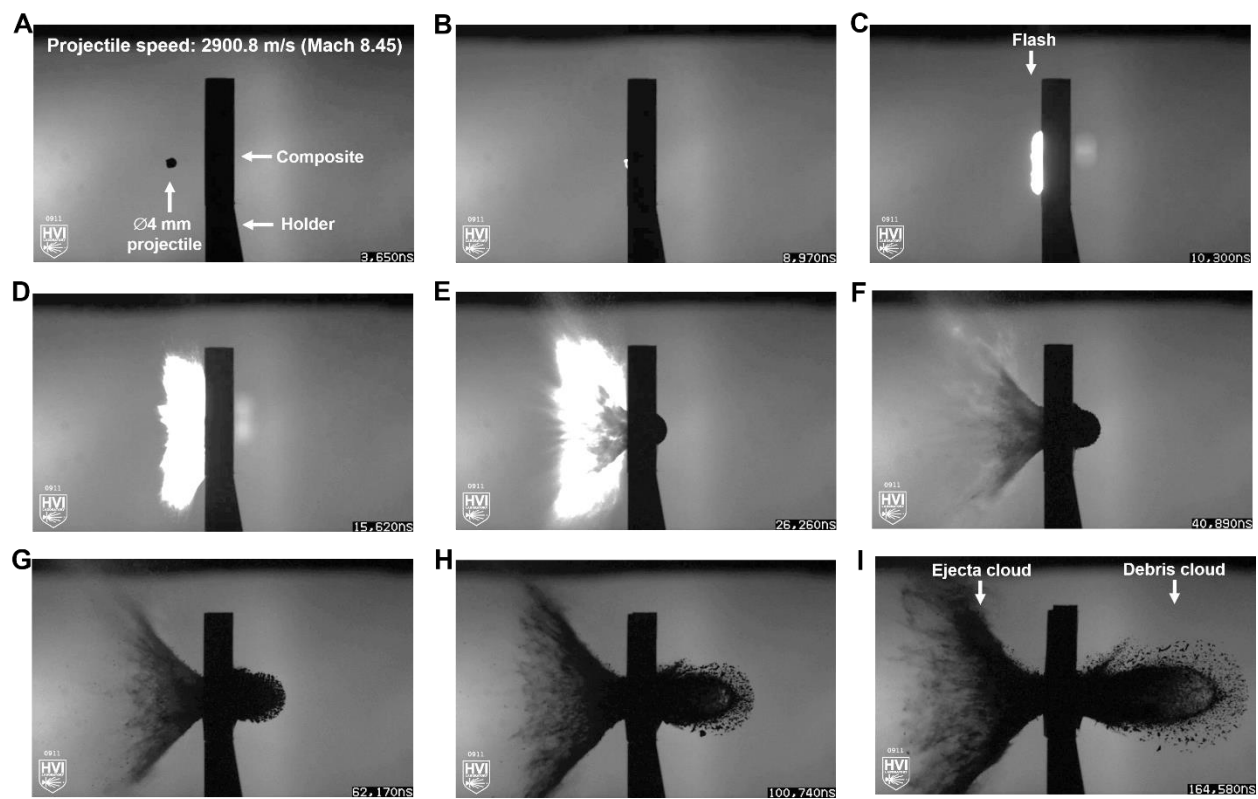


**Fig. S12. Shadowgraphs of the impact test with  $\varnothing 4$  mm projectile (speed 2900.8 m/s, Mach 8.45). (A-I)** High-contrast shadowgraphs of the impact event at different time-scales with one  $\varnothing 4$  mm aluminum spherical projectile.

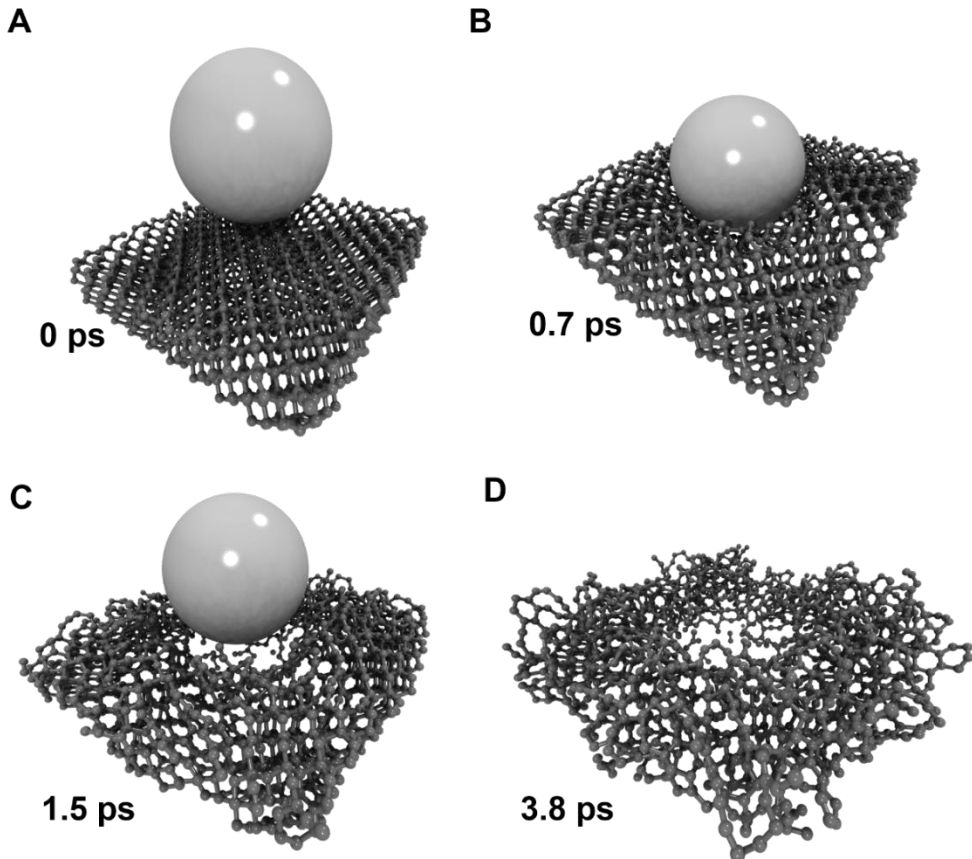


**Fig. S13. Time evolution of the projectile's impact on the diamond surface. (A-D)**

Time evolution of the impacted diamond surface at different simulation times: 0 ps, 0.7 ps, 1.5 ps, and 3.8 ps. At the initial stage (0 ps), the system exhibits a perfectly ordered crystalline structure, corresponding to the equilibrium state after thermal relaxation. At 0.7 ps, the collision and the subsequent penetration phase occur. The projectile's kinetic energy is rapidly converted into potential and thermal energy, generating a compressive shock wave that propagates through the diamond lattice. This initial compression induces the formation of local defects and atomic displacements, particularly in regions of high stress accumulation. At 1.5 ps, the target surface exhibits significant plastic deformation and increased local roughness. The energy transfer leads to the breaking of covalent  $sp^3$  bonds and to a partial conversion to  $sp^2$  ones, resulting in a structurally disordered region. The accumulation of shear stresses around the impact zone promotes the nucleation of amorphous regions and the loss of crystalline symmetry. By 3.8 ps, the diamond undergoes a pronounced structural transition: the material surrounding the crater exhibits a partial collapse of the lattice, forming an amorphous, highly damaged region, while the inner layers retain minor remnants of tetrahedral order and a considerable fraction of  $sp^2$ -hybridized carbon atoms.

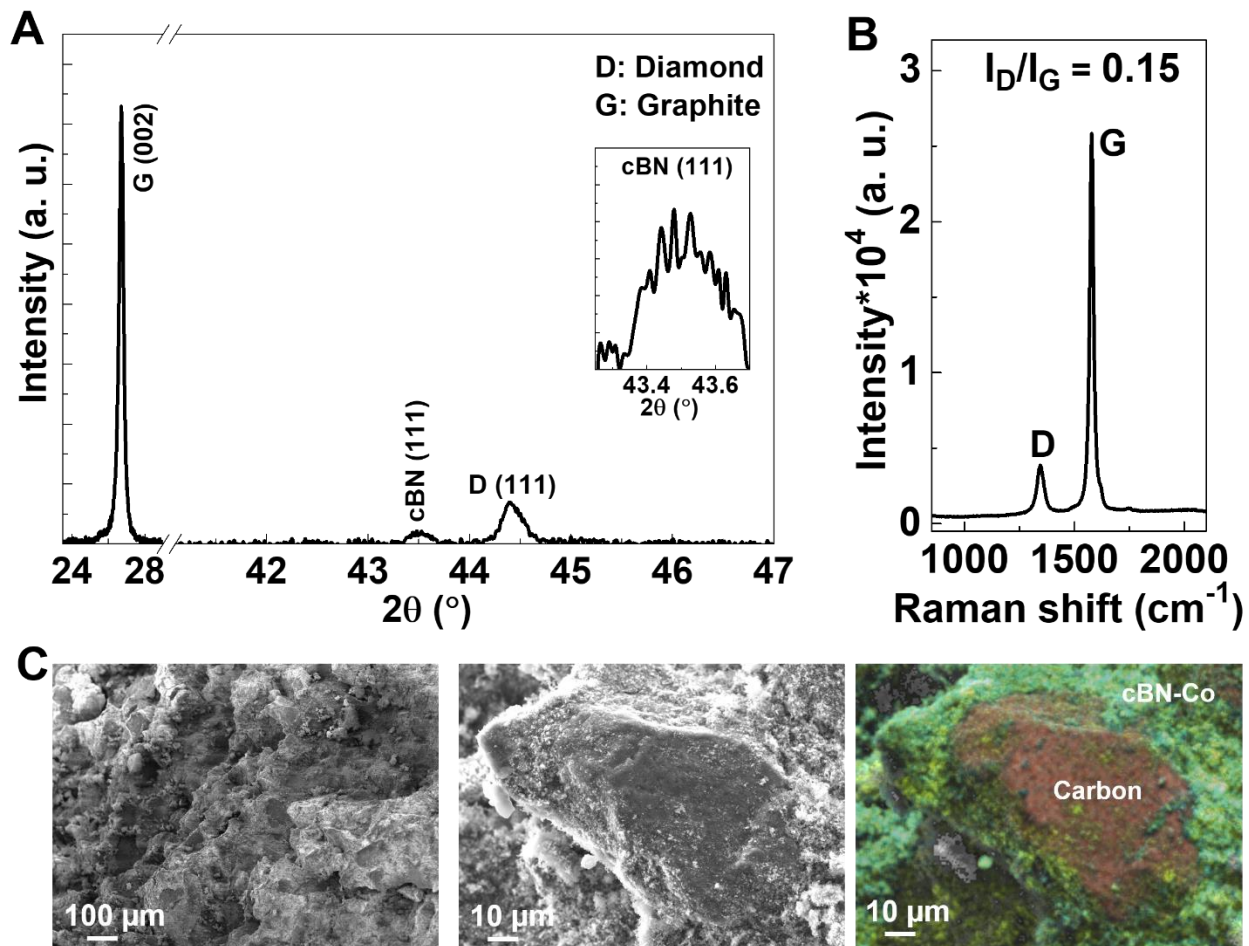


**Fig. S14. Characterizations of the composite after the Ø1 mm projectile impact test.** (A) XRD shows the formation of graphite along with the presence of cBN and diamond phases. (B) Raman spectroscopy also shows the graphitization with disorder. (C) FESEM morphology and the elemental map showing carbon and cBN-Co regions.

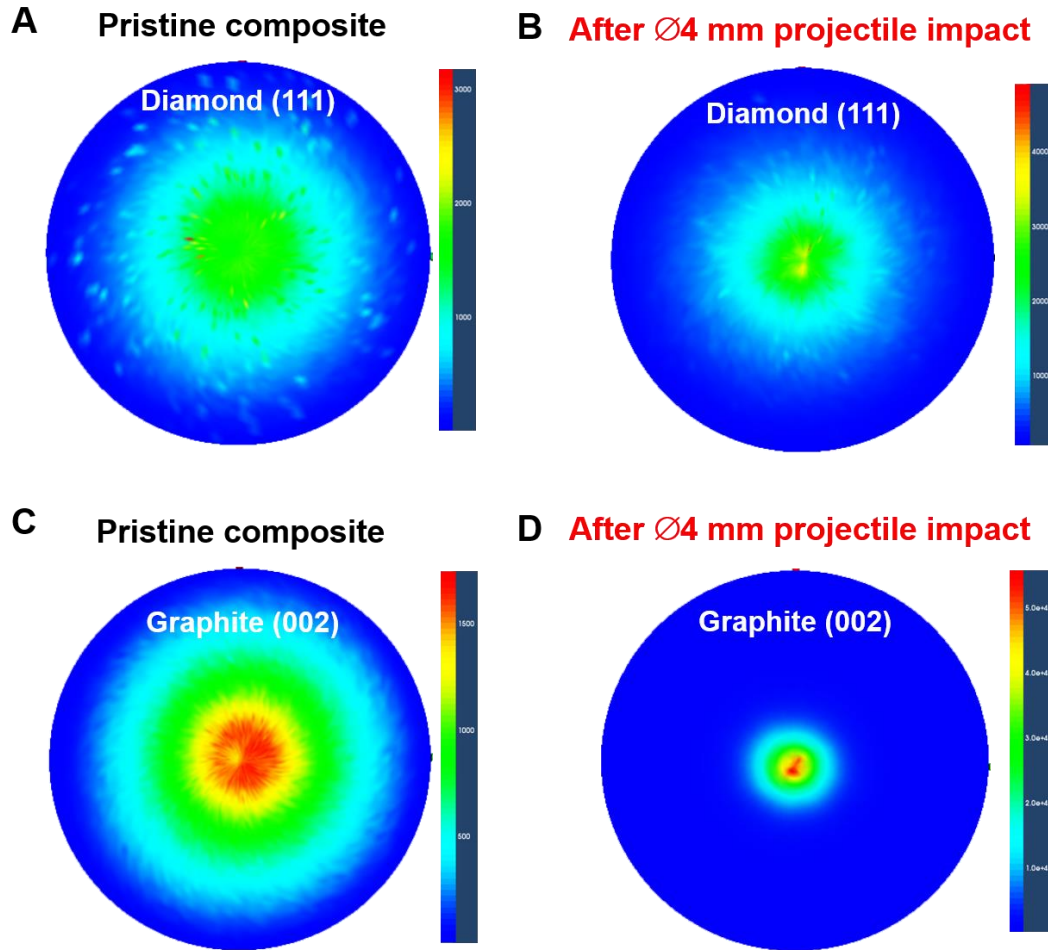


**Fig. S15. Pole figure map of the composite after the  $\varnothing 4$  mm projectile impact test.** (A and B) XRD pole figure map of the (111) diamond peak. (C and D) XRD pole figure map of the (002) graphite peak of the composite. For pristine composite, the diamond particles are oriented with (111) facets along random directions. In contrast, phase transformed graphite becomes mostly oriented along (002) after the impact.

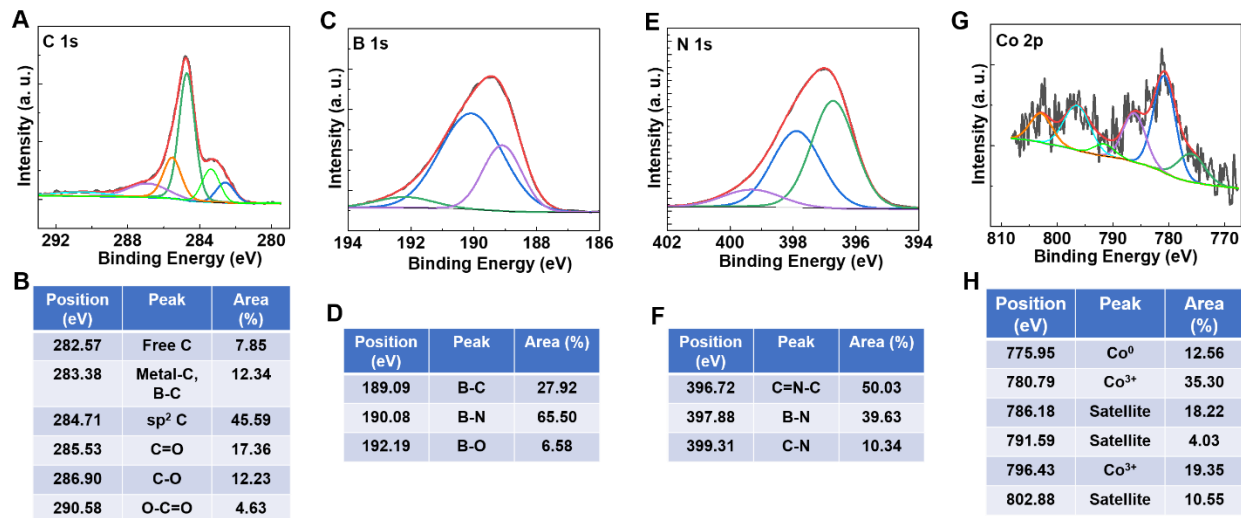


**Fig. S16. XPS of the composite after the Ø4 mm projectile impact test.** Core-level elemental XPS sans and their fittings show various possible bonding for (A and B) C 1s, (C and D) B 1s, (E and F) N 1s, and (G and H) Co 2p.

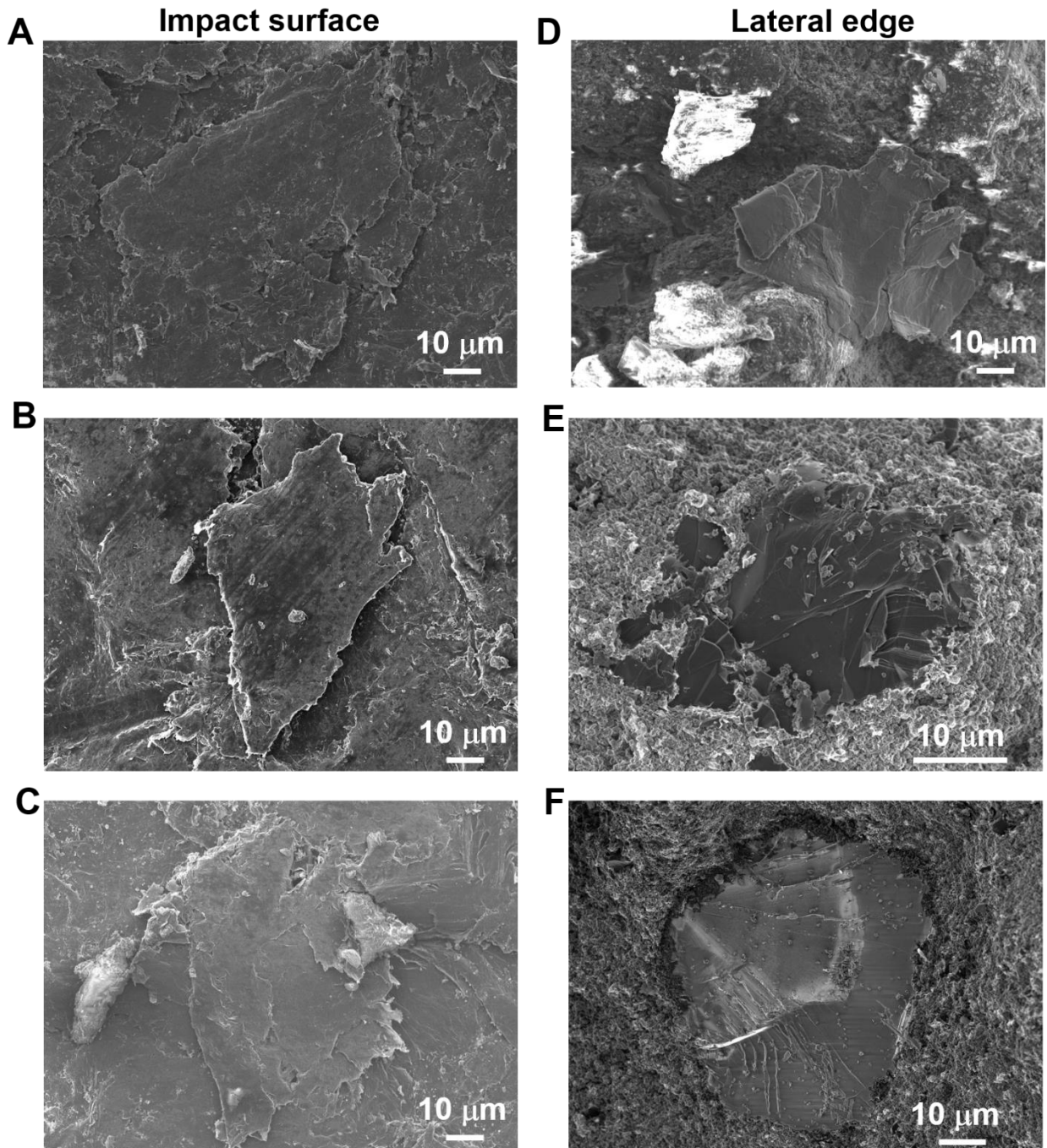


**Fig. S17. FESEM surface morphology after the  $\varnothing 4$  mm projectile impact test. (A-C)**  
 It shows the graphitic layers from the impact surface of the shattered disk (the side on which the projectile impacted). **(D-F)** It shows the graphitic layer from the fractured lateral edge of the disk. Images from both sides undoubtably confirm the formation of graphitic layers throughout the bulk of the composite, after the  $\varnothing 4$  mm projectile impact (as similarly seen through XRM imaging).

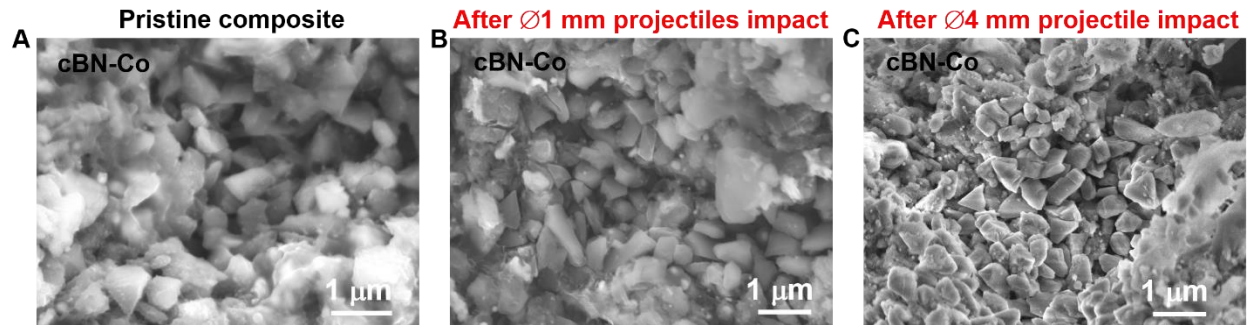


**Fig. S18. Presence of cBN in diamond-cBN-Co composites.** FESEM morphology in (A) pristine and (B and C) after impact composites showing cBN particles, as similarly for the pristine cBN powder (as shown in **fig. S1B**).

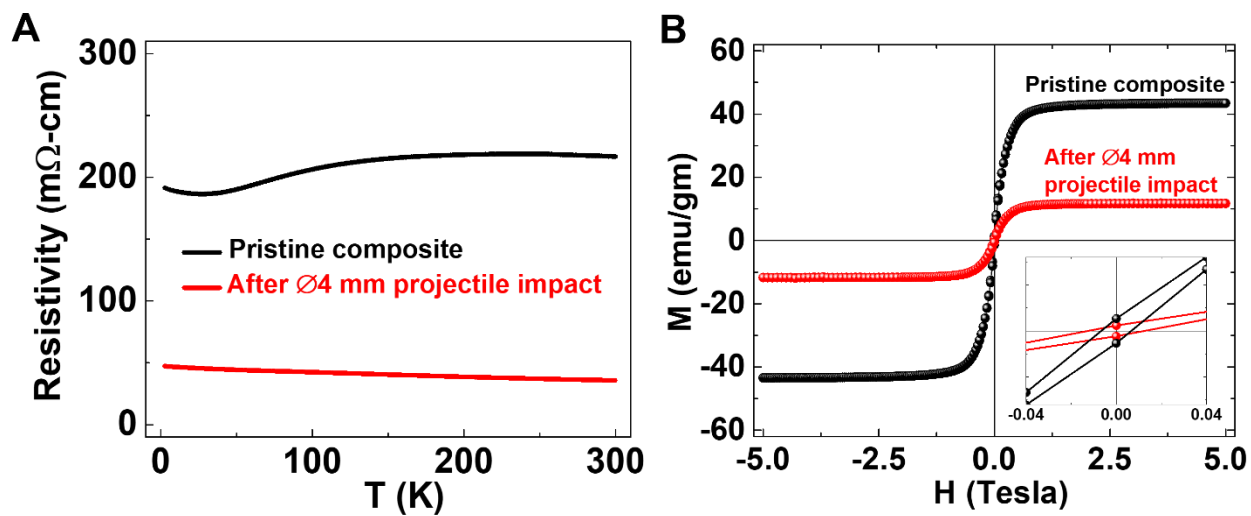


**Fig. S19. Electrical transport and magnetic properties of the composite after the Ø4 mm projectile impact test.** (A) Considering the more graphitic nature of the composite, electrical resistivity decreased with a value of  $\sim 36$  mΩ·cm at room temperature. (B) It still retains a ferromagnetic behavior at room temperature, however with reduced magnetic moments.

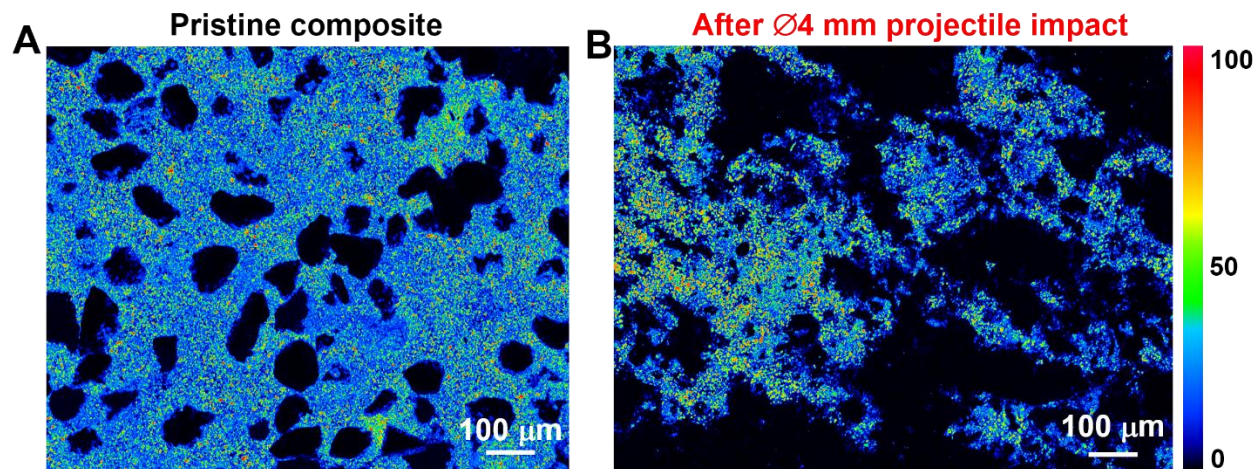


**Fig. S20. WDS elemental map of Co in the Ø4 mm projectile-impacted composite.**  
(A and B) Within the random region of analysis, we found Co ~30.88 wt% in the pristine composite, whereas Co ~13.62 wt% in the after Ø4 mm impact sample.

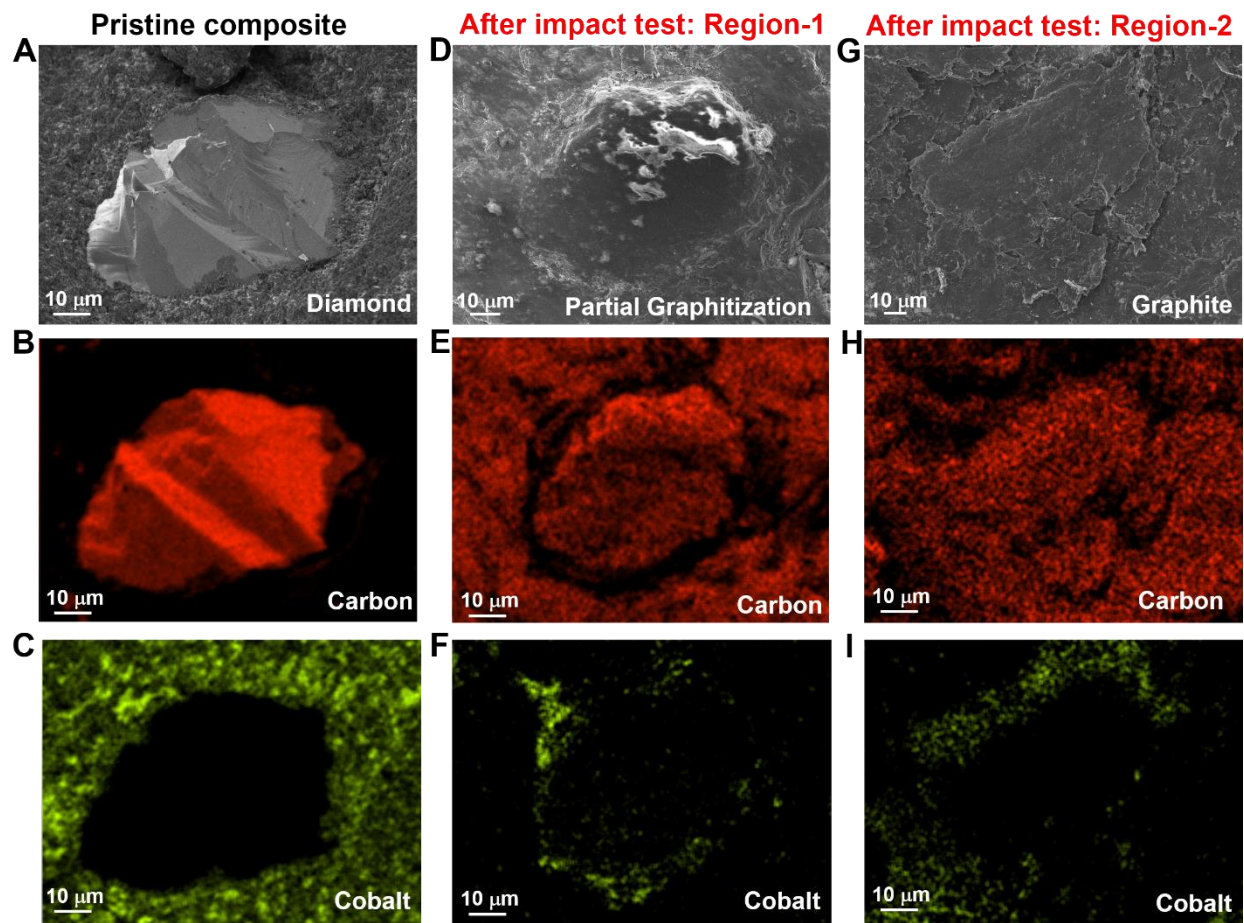


**Fig. S21. Morphological comparison of the diamond particle in the pristine composite and after the  $\varnothing 4$  mm projectile impact.** (A, D, and G) FESEM surface morphology of a typical diamond particle, which shows that in some cases it's partially graphitized (forming a diamond-graphite region) whereas in some cases it forms fully graphitic layers. (B, E, and H) Corresponding EDS maps showing carbon and (C, F, and I) Co particles, surrounded by the diamond/graphitic regions.

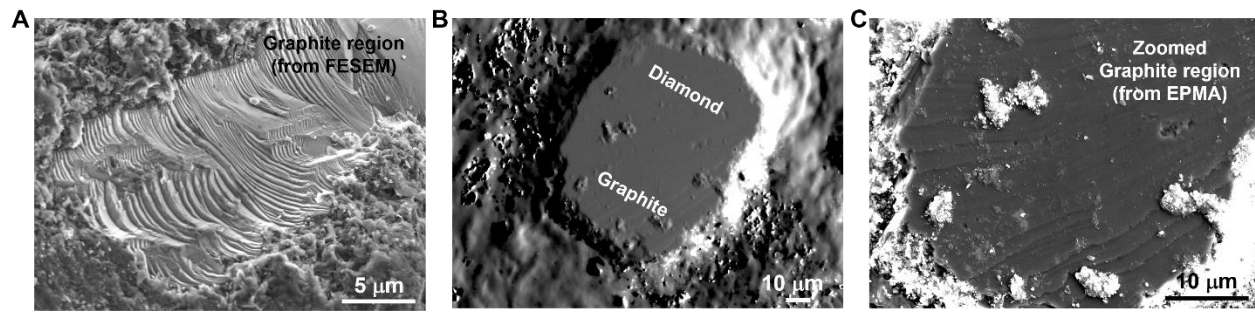


**Fig. S22. Zoomed-in morphology of diamond grains in the composite after the  $\varnothing 4$  mm projectile impact test.** Zoomed-in (A) FESEM morphology and (B and C) EMPA topography of the diamond grain, showing the formation of layered sheet-like texture at lower regions (zoomed in lower graphitic region in B).

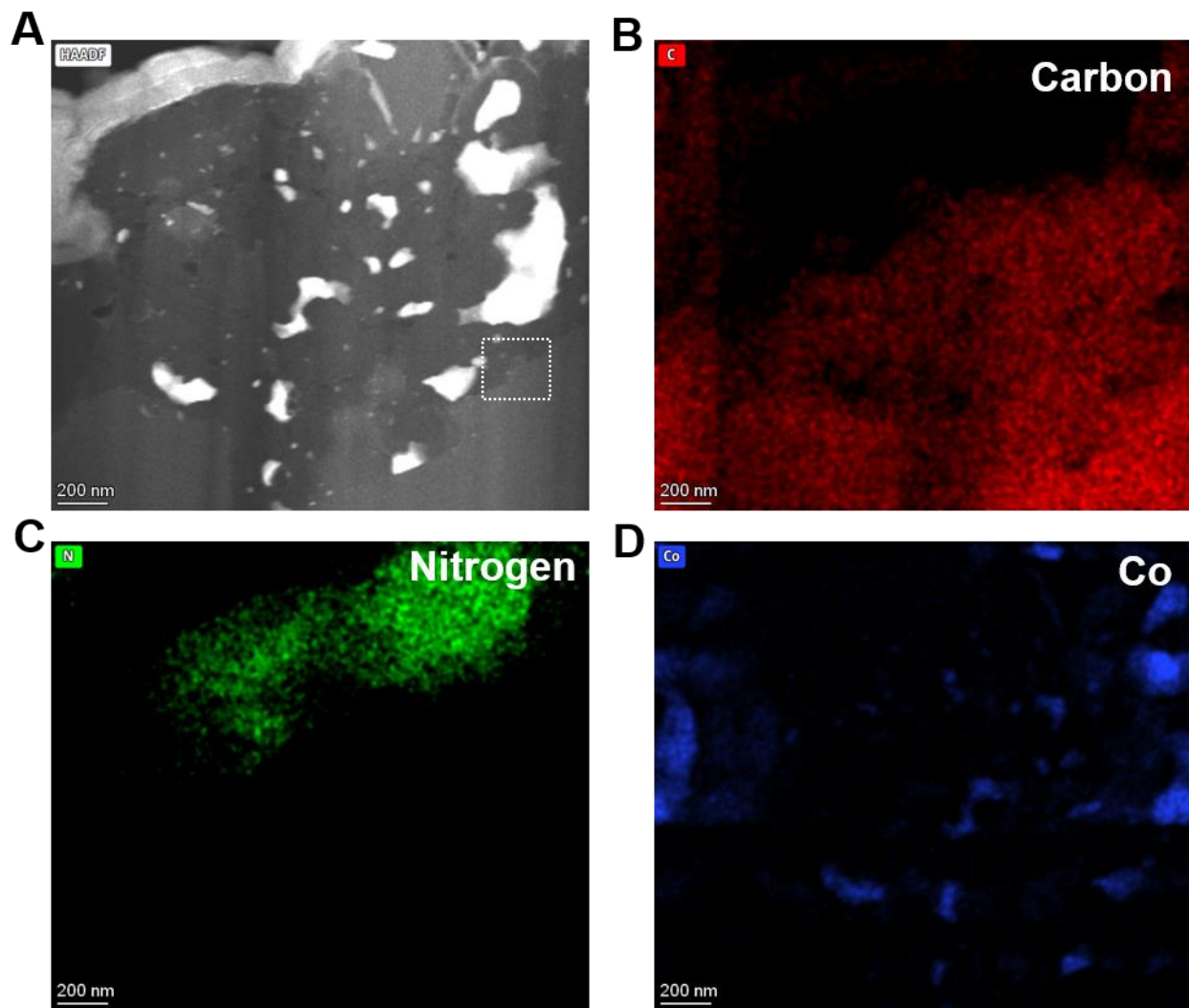


**Fig. S23. Chemical composition mapping by STEM EDX.** (A) Cross-sectional HAADF-STEM image of the after-impact sample. White dashed box is the region where the atomic-scale interface image is shown in the main. (B-D) EDX mapping showing the presence of C, N, and Co.

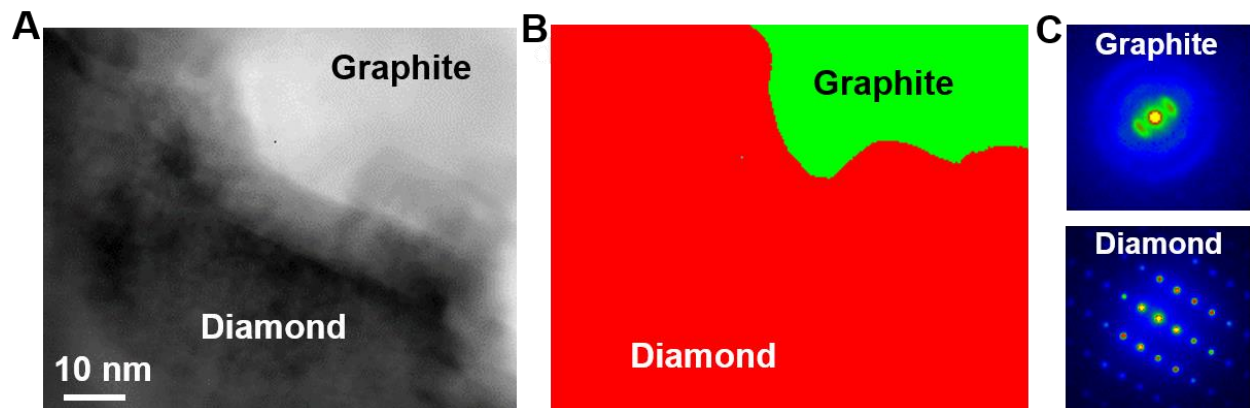


**Fig. S24. Interface between diamond and graphite.** (A) Virtual Bright-field STEM image of diamond-graphite interface. (B and C) Precession 4D-STEM phase mapping and corresponding diffraction patterns from the respective region showing [211] and [110] orientations of diamond and graphite.

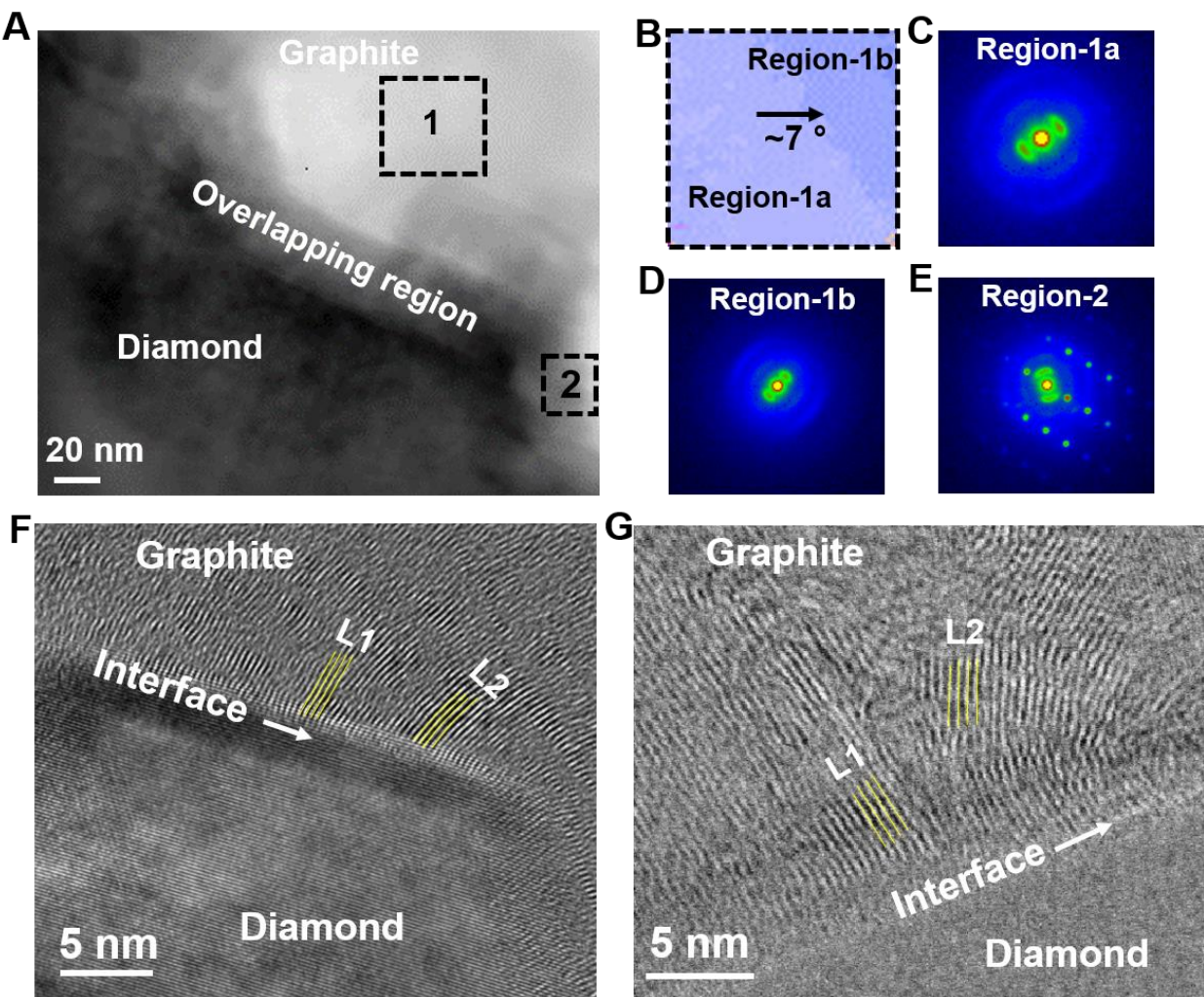


**Fig. S25. 4D-STEM of the diamond-graphite interface.** (A) Virtual bright-field STEM image of the diamond-graphite interface and the overlapped regions. (B) Within the black dashed region, it reveals misorientation mapping of graphite layers ( $\sim 7^\circ$ ). Corresponding 4D STEM diffraction patterns are shown (C) from Region-1a, (D) from Region-1b, and (E) from Region-2. Region-2 shows the presence of both diamond and graphite which is the overlapped region. (F) HRTEM shows  $\sim 7^\circ$  misoriented graphitic layers starting from layer L1 to layer L2 (yellow lines). (G) ABF STEM shows other misoriented graphitic layers with an angle between the layer L1 and L2 of  $32^\circ$ , from a random interface region.

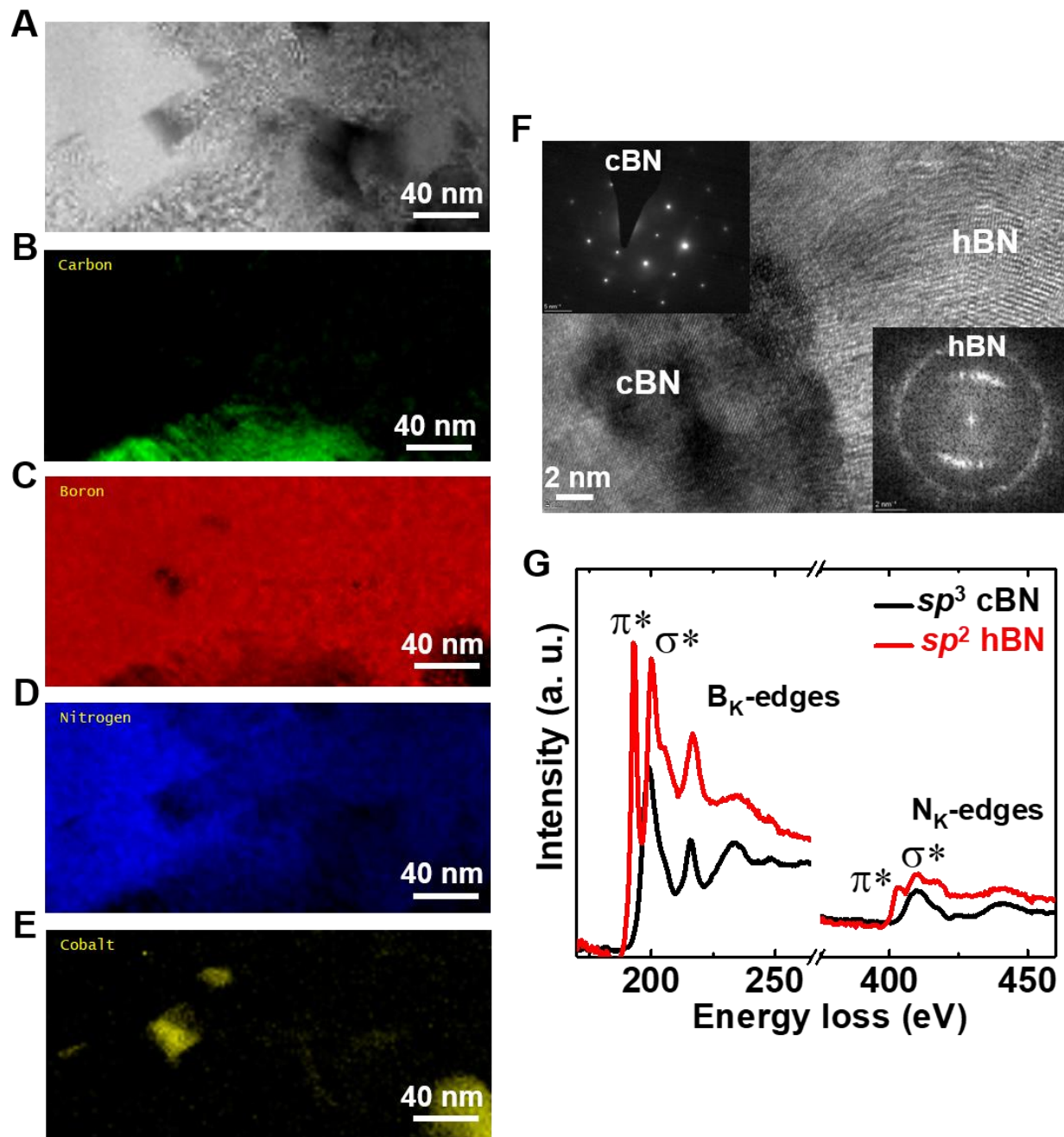


**Fig. S26. HRTEM imaging and STEM EELS of the BN region in the composite after the Ø4 mm projectile impact. (A) ADF STEM image and (B-E) corresponding EELS map showing the presence of C, B, N, and Co. (F) HRTEM along with the FFTs showing the presence of cBN and hBN. (G) STEM-EELS spectra from the  $sp^3$  cBN and  $sp^2$  hBN regions.**

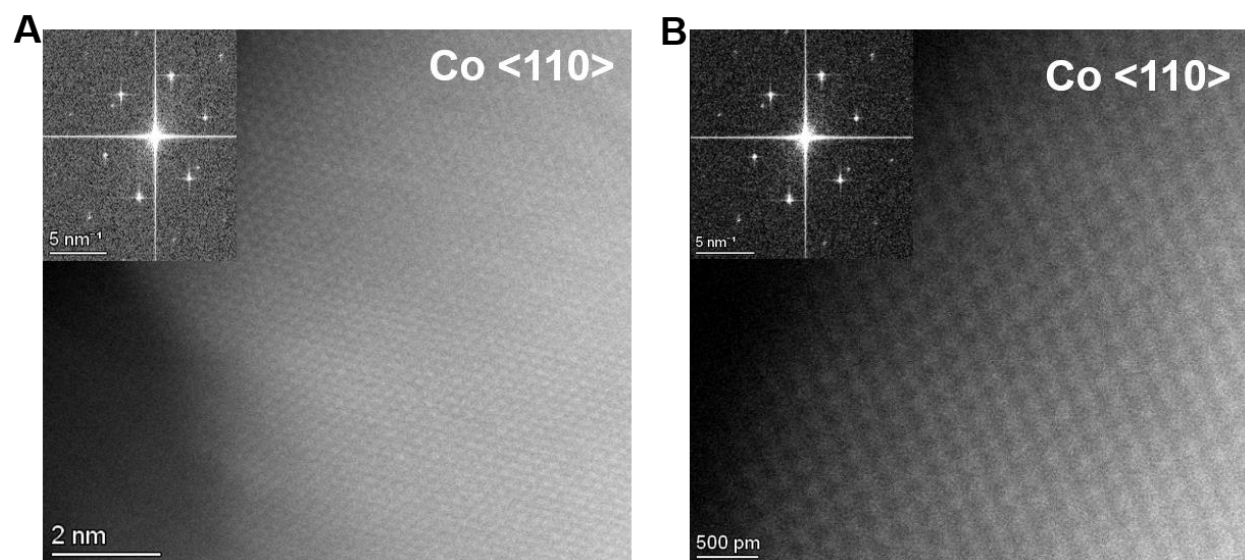


**Fig. S27. TEM images of Co in the composite after the Ø4 mm projectile impact test.**  
**(A and B)** HR-STEM and the FFTs pattern showing  $<110>$  orientation of cubic Co lattice from different region of the sample.



**Fig. S28. Hypervelocity impact test facility.** An overview of the two-stage light-gas gun (2SLGG) at the Texas A&M University (TAMU, USA) Hypervelocity Impact Laboratory (HVIL). The key components include: gun powder breech, pump tube, central breech, nominally 12.7 mm diameter smooth-bore launch tube, blast tank, drift tube with laser velocimetry system, and target tank. The gunpowder loading occurs at the uprange end, while the projectile impacts the composite sample in the target tank located downrange.

## Supplementary Tables

**Table S1. Elements analyzed by EPMA:** Spectrometer conditions: X-ray lines, standards used, peak position, and background offsets

Element	X-ray	Analyzing Crystal	Standard	Peak Pos. (L-value) (mm)	Lower Backgr. offset (mm)	Upper Backgr. offset (mm)
C	K <sub>α</sub>	LDE2	C_graphite_SPI	127.464	6	5
B	K <sub>α</sub>	LDE2	BN_SPI	194.516	6	5
N	K <sub>α</sub>	LDE1	BN_SPI	147.201	5	5
Co	K <sub>α</sub>	LIFL	Co_SPI	124.515	5	5

**Table S2. Detector conditions for EPMA analysis:** counting time (Peak=P<sub>k</sub> and background = B<sub>k</sub>) and detector conditions.

Element	P <sub>k</sub> counting (sec)	B <sub>k</sub> counting (sec)	Peak search	Mass (%)	Detector conditions				
					Gain	High.V (V)	Base Line (V)	Window (V)	Mode
C	10	5	Yes	99.99	64	1700	0.7	9.3 (V)	Dif
B	10	5	Yes	43.6	64	1700	0.7	9.3 (V)	Dif
N	10	5	No	56.44	64	1645	1.4	8.7 (V)	Dif
Co	10	5	Yes	99.995	16	1612	0.7	0	Int

## Supplementary Text

To identify the hexagonal regions (main **Fig. 2K**) formed during graphitization induced by projectile impact, a geometric-topological procedure was applied to the final configuration of the MD simulation. Atomic bonds were defined exclusively using a geometric criterion, in which two atoms were considered bonded if their interatomic distance was smaller than a cutoff value fixed at 1.7 Å. Based on this criterion, an undirected atomic connectivity graph was constructed, with vertices representing atoms and edges corresponding to local bonds. To distinguish graphitic domains from remnant diamond structures, a topological filter based on atomic coordination was applied, excluding from the ring analysis all atoms with coordination numbers greater than three, which are characteristic of the tetrahedral  $sp^3$  bonding network of diamond.

Ring detection was then performed on the resulting subgraph containing only atoms with coordination numbers less than or equal to three. Simple cycles of length six were explicitly identified using a depth-first search (DFS) algorithm constrained to closed paths composed of six distinct vertices, ensuring the detection of genuine hexagonal rings typical of graphitic structures. Additional pruning strategies were employed to prevent redundant detections by enforcing an ordering constraint on the initial vertices of the cycles. All atoms participating in at least one identified six-membered ring were classified as belonging to hexagonal regions, whose spatial distribution is highlighted (**Fig. 2K**).

## References

1. Q. Huang, D. Yu, B. Xu, W. Hu, Y. Ma, Y. Wang, Z. Zhao, B. Wen, J. He, Z. Liu, Y. Tian, Nanotwinned diamond with unprecedented hardness and stability. *Nature* **510**, 250–253 (2014).
2. T. Irifune, A. Kurio, S. Sakamoto, T. Inoue, H. Sumiya, Ultrahard polycrystalline diamond from graphite. *Nature* **421**, 599–600 (2003).
3. J. E. Graebner, S. Jin, G. W. Kammlott, J. A. Herb, C. F. Gardinier, Large anisotropic thermal conductivity in synthetic diamond films. *Nature* **359**, 401–403 (1992).
4. X. Guo, M. Xie, A. Addhya, A. Linder, U. Zvi, S. Wang, X. Yu, T. D. Deshmukh, Y. Liu, I. N. Hammock, Z. Li, C. T. DeVault, A. Butcher, A. P. Esser-Kahn, D. D. Awschalom, N. Delegan, P. C. Maurer, F. J. Heremans, A. A. High, Direct-bonded diamond membranes for heterogeneous quantum and electronic technologies. *Nat Commun* **15**, 8788 (2024).
5. J. E. Field, The mechanical and strength properties of diamond. *Rep. Prog. Phys.* **75**, 126505 (2012).
6. A. Nie, Z. Zhao, B. Xu, Y. Tian, Microstructure engineering in diamond-based materials. *Nat. Mater.* **24**, 1172–1185 (2025).
7. F. P. Bundy, H. T. Hall, H. M. Strong, R. H. Wentorfjun., Man-Made Diamonds. *Nature* **176**, 51–55 (1955).
8. S. Ferro, Synthesis of diamond. *J. Mater. Chem.* **12**, 2843–2855 (2002).
9. Y. Gong, D. Luo, M. Choe, Y. Kim, B. Ram, M. Zafari, W. K. Seong, P. Bakharev, M. Wang, I. K. Park, S. Lee, T. J. Shin, Z. Lee, G. Lee, R. S. Ruoff, Growth of diamond in liquid metal at 1 atm pressure. *Nature* **629**, 348–354 (2024).
10. J. Zhang, J. Wang, G. Zhang, Z. Huo, Z. Huang, L. Wu, A review of diamond synthesis, modification technology, and cutting tool application in ultra-precision machining. *Materials & Design* **237**, 112577 (2024).
11. J. Jing, F. Sun, Z. Wang, L. Ma, Y. Luo, Z. Du, T. Zhang, Y. Wang, F. Xu, T. Zhang, C. Chen, X. Ma, Y. He, Y. Zhu, H. Sun, X. Wang, Y. Zhou, J. K. H. Tsoi, J. Wrachtrup, N. Wong, C. Li, D.-K. Ki, Q. Wang, K. H. Li, Y. Lin, Z. Chu, Scalable production of ultraflat and ultraflexible diamond membrane. *Nature* **636**, 627–634 (2024).
12. J. Tu, J. Li, Y. Wang, Y. Zhao, J. Liu, J. Wei, L. Chen, J. Zhang, Y. Lu, C. Li, Inch-scale ultrahard diamond wafer with 200 GPa hardness via high-frequency pulsed local non-equilibrium growth. *Nat. Commun.*, **16**, 11303 (2025).
13. M. Seal, Graphitization and Plastic Deformation of Diamond. *Nature* **182**, 1264–1267 (1958).

14. M. Seal, Graphitization of Diamond. *Nature* **185**, 522–523 (1960).
15. G. Davies, T. Evans, Graphitization of diamond at zero pressure and at a high pressure. *Proc. A* **328** (1574): 413–427 (1972).
16. Y. G. Gogotsi, A. Kailer, K. G. Nickel, Transformation of diamond to graphite. *Nature* **401**, 663–664 (1999).
17. S. N. Monteiro, A. L. D. Skury, M. G. de Azevedo, G. S. Bobrovitchii, Cubic boron nitride competing with diamond as a superhard engineering material – an overview. *Journal of Materials Research and Technology* **2**, 68–74 (2013).
18. Y. Tian, B. Xu, D. Yu, Y. Ma, Y. Wang, Y. Jiang, W. Hu, C. Tang, Y. Gao, K. Luo, Z. Zhao, L.-M. Wang, B. Wen, J. He, Z. Liu, Ultrahard nanotwinned cubic boron nitride. *Nature* **493**, 385–388 (2013).
19. Y. N. Palyanov, Y. M. Borzdov, I. N. Kupriyanov, A. F. Khokhryakov, D. V. Nechaev, Rare-earth metal catalysts for high-pressure synthesis of rare diamonds. *Sci Rep* **11**, 8421 (2021).
20. Y. Tian, J. Wang, J. Zhang, S. Guan, L. Zhang, B. Wu, Y. Su, M. Huang, L. Zhou, D. He, Solubility and stability of diamond in cobalt under 5 GPa. *Diamond and Related Materials* **110**, 108158 (2020).
21. K. Chen, B. Song, N. K. Ravichandran, Q. Zheng, X. Chen, H. Lee, H. Sun, S. Li, G. A. G. U. Gamage, F. Tian, Z. Ding, Q. Song, A. Raj, H. Wu, P. Koirala, A. J. Schmidt, K. Watanabe, B. Lv, Z. Ren, L. Shi, D. G. Cahill, T. Taniguchi, D. Broido, G. Chen, Ultrahigh thermal conductivity in isotope-enriched cubic boron nitride. *Science* **367**, 555-559 (2020).
22. F. P. Bundy, Diamond Synthesis with Non-conventional Catalyst-solvents. *Nature* **241**, 116–118 (1973).
23. A. R. Badzian, A. Klokocki, On the catalytic growth of synthetic diamonds. *Journal of Crystal Growth* **52**, 843–847 (1981).
24. A. De Vita, G. Galli, A. Canning, R. Car, A microscopic model for surface-induced diamond-to-graphite transitions. *Nature* **379**, 523–526 (1996).
25. K. Luo, B. Liu, W. Hu, X. Dong, Y. Wang, Q. Huang, Y. Gao, L. Sun, Z. Zhao, Y. Wu, Y. Zhang, M. Ma, X.-F. Zhou, J. He, D. Yu, Z. Liu, B. Xu, Y. Tian, Coherent interfaces govern direct transformation from graphite to diamond. *Nature* **607**, 486–491 (2022).
26. H. Zhang, Z. Yan, H. Zhang, G. Chen, Graphitization of diamond: manifestations, mechanisms, influencing factors and functional applications. *Functional Diamond* **5**, 2533896 (2025).

27. E. O'Bannon, G. Xia, F. Shi, R. Wirth, A. King, L. Dobrzhinetskaya, The transformation of diamond to graphite: Experiments reveal the presence of an intermediate linear carbon phase. *Diamond and Related Materials* **108**, 107876 (2020).

28. R. A. Khmelnitsky, A. A. Gippius, Transformation of diamond to graphite under heat treatment at low pressure. *Phase Transitions* **87**, 175-192 (2014).

29. B. B. Bokhonov, D. V. Dudina, M. R. Sharafutdinov, Graphitization of synthetic diamond crystals: A morphological study. *Diamond and Related Materials* **118**, 108563 (2021).

30. X. Yan, J. Wei, K. An, J. Liu, L. Chen, Y. Zheng, X. Zhang, C. Li, High temperature surface graphitization of CVD diamond films and analysis of the kinetics mechanism. *Diamond and Related Materials* **120**, 108647 (2021).

31. B. Ali, H. Xu, D. Chetty, R. T. Sang, I. V. Litvinyuk, M. Rybachuk, Laser-Induced Graphitization of Diamond Under 30 fs Laser Pulse Irradiation. *J. Phys. Chem. Lett.* **13**, 2679–2685 (2022).

32. D. Saada, J. Adler, R. Kalish, Transformation of Diamond (sp3) to Graphite (sp2) Bonds by Ion-Impact. *Int. J. Mod. Phys. C* **09**, 61–69 (1998).

33. D. P. Hickey, K. S. Jones, R. G. Elliman, Amorphization and graphitization of single-crystal diamond — A transmission electron microscopy study. *Diamond and Related Materials* **18**, 1353–1359 (2009).

34. D. J. Erskine, W. J. Nellis, Shock-induced martensitic phase transformation of oriented graphite to diamond. *Nature* **349**, 317–319 (1991).

35. G.-W. Chen, S.-C. Zhu, L. Xu, Y.-M. Li, Z.-P. Liu, Y. Hou, H. Mao, The Transformation Mechanism of Graphite to Hexagonal Diamond under Shock Conditions. *JACS Au* **4**, 3413–3420 (2024).

36. T. Evans, P. F. James, A study of the transformation of diamond to graphite. *Proc. A* **277**, 260–269 (1964).

37. S. Eswarappa Prameela, T. M. Pollock, D. Raabe, M. A. Meyers, A. Aitkaliyeva, K.-L. Chintersingh, Z. C. Cordero, L. Graham-Brady, Materials for extreme environments. *Nat Rev Mater* **8**, 81–88 (2023).

38. Z. Li, Y. Wang, M. Ma, H. Ma, W. Hu, X. Zhang, Z. Zhuge, S. Zhang, K. Luo, Y. Gao, L. Sun, A. V. Soldatov, Y. Wu, B. Liu, B. Li, P. Ying, Y. Zhang, B. Xu, J. He, D. Yu, Z. Liu, Z. Zhao, Y. Yue, Y. Tian, X. Li, Ultrastrong conductive *in situ* composite composed of nanodiamond incoherently embedded in disordered multilayer graphene. *Nat. Mater.* **22**, 42–49 (2023).

39. P. Németh, K. McColl, L. A. J. Garvie, C. G. Salzmann, M. Murri, P. F. McMillan, Complex nanostructures in diamond. *Nat. Mater.* **19**, 1126–1131 (2020).

40. Y. Yue, Y. Gao, W. Hu, B. Xu, J. Wang, X. Zhang, Q. Zhang, Y. Wang, B. Ge, Z. Yang, Z. Li, P. Ying, X. Liu, D. Yu, B. Wei, Z. Wang, X.-F. Zhou, L. Guo, Y. Tian, Hierarchically structured diamond composite with exceptional toughness. *Nature* **582**, 370–374 (2020).

41. B. Li, P. Ying, Y. Gao, W. Hu, L. Wang, Y. Zhang, Z. Zhao, D. Yu, J. He, J. Chen, B. Xu, Y. Tian, Heterogeneous Diamond-cBN Composites with Superb Toughness and Hardness. *Nano Lett.* **22**, 4979–4984 (2022).

42. A. C. Li, B. Li, F. González-Cataldo, R. E. Rudd, B. Militzer, E. M. Bringa, M. A. Meyers, Diamond under extremes. *Materials Science and Engineering: R: Reports* **161**, 100857 (2024).

43. A. B. Peters, D. Zhang, S. Chen, C. Ott, C. Oses, S. Curtarolo, I. McCue, T. M. Pollock, S. Eswarappa Prameela, Materials design for hypersonics. *Nat Commun* **15**, 3328 (2024).

44. H. Wei, H. Zhan, D. Legut, S. Zhang, A dislocation perspective on heterointerfacial strengthening in nanostructured diamond and cubic boron nitride composites. *Carbon* **235**, 120079 (2025).

45. R. Qi, R. Shi, Y. Li, Y. Sun, M. Wu, N. Li, J. Du, K. Liu, C. Chen, J. Chen, F. Wang, D. Yu, E.-G. Wang, P. Gao, Measuring phonon dispersion at an interface. *Nature* **599**, 399–403 (2021).

46. H. G. Johnson, S. P. Bennett, R. Barua, L. H. Lewis, D. Heiman, Universal properties of linear magnetoresistance in strongly disordered MnAs-GaAs composite semiconductors. *Phys. Rev. B* **82**, 085202 (2010).

47. C. E. Anderson, T. G. Trucano, S. A. Mullin, Debris cloud dynamics. *International Journal of Impact Engineering* **9**, 89–113 (1990).

48. A. J. Piekutowski, Characteristics of debris clouds produced by hypervelocity impact of aluminum spheres with thin aluminum plates. *International Journal of Impact Engineering* **14**, 573–586 (1993).

49. B. G. Cour-Palais, Hypervelocity impact in metals, glass and composites. *International Journal of Impact Engineering* **5**, 221–237 (1987).

50. L. C. Liang, Carbon K $\alpha$  peak shift study using an electron probe microanalyzer with a vanadium–carbon multilayer pseudo-crystal. *X-Ray Spectrometry* **21**, 191–192 (1992).

51. M. N. R. Ashfold, J. P. Goss, B. L. Green, P. W. May, M. E. Newton, C. V. Peaker, Nitrogen in Diamond. *Chem. Rev.* **120**, 5745–5794 (2020).

52. J. L. Pouchou, F. Pichoir, Electron Probe X-Ray Microanalysis Applied to Thin Surface Films and Stratified Specimens. *Scanning Microscopy* **1993** (1993).

53. Y. Guo, T. Staedler, J. Müller, S. Heuser, B. Butz, X. Jiang, A detailed analysis of the determination of fracture toughness by nanoindentation induced radial cracks. *Journal of the European Ceramic Society* **40**, 276–289 (2020).

54. M. Sebastiani, K. E. Johanns, E. G. Herbert, G. M. Pharr, Measurement of fracture toughness by nanoindentation methods: Recent advances and future challenges. *Current Opinion in Solid State and Materials Science* **19**, 324–333 (2015).

55. J. A. Rogers, N. Bass, P. T. Mead, A. Mote, G. D. Lukasik, M. Intardonato, K. Harrison, J. D. Leaverton, K. R. Kota, J. W. Wilkerson, J. N. Reddy, W. D. Kulatilaka, T. E. Lacy Jr., The Texas A&M University Hypervelocity Impact Laboratory: A modern aeroballistic range facility. *Rev. Sci. Instrum.* **93**, 085106 (2022).

56. G. Henkelman, B. P. Uberuaga, H. Jónsson, A climbing image nudged elastic band method for finding saddle points and minimum energy paths. *J. Chem. Phys.* **113**, 9901–9904 (2000).

57. B. Hourahine, B. Aradi, V. Blum, F. Bonafé, A. Buccheri, C. Camacho, C. Cevallos, M. Y. Deshaye, T. Dumitrică, A. Dominguez, S. Ehlert, M. Elstner, T. van der Heide, J. Hermann, S. Irle, J. J. Kranz, C. Köhler, T. Kowalczyk, T. Kubař, I. S. Lee, V. Lutsker, R. J. Maurer, S. K. Min, I. Mitchell, C. Negre, T. A. Niehaus, A. M. N. Niklasson, A. J. Page, A. Pecchia, G. Penazzi, M. P. Persson, J. Řezáč, C. G. Sánchez, M. Sternberg, M. Stöhr, F. Stuckenberg, A. Tkatchenko, V. W. -z. Yu, T. Frauenheim, DFTB+, a software package for efficient approximate density functional theory based atomistic simulations. *J. Chem. Phys.* **152**, 124101 (2020).

58. A. Hjorth Larsen, J. Jørgen Mortensen, J. Blomqvist, I. E. Castelli, R. Christensen, M. Dułak, J. Friis, M. N. Groves, B. Hammer, C. Hargus, E. D. Hermes, P. C. Jennings, P. Bjerre Jensen, J. Kermode, J. R. Kitchin, E. Leonhard Kolsbjerg, J. Kubal, K. Kaasbjerg, S. Lysgaard, J. Bergmann Maronsson, T. Maxson, T. Olsen, L. Pastewka, A. Peterson, C. Rostgaard, J. Schiøtz, O. Schütt, M. Strange, K. S. Thygesen, T. Vegge, L. Vilhelmsen, M. Walter, Z. Zeng, K. W. Jacobsen, The atomic simulation environment—a Python library for working with atoms. *J. Phys.: Condens. Matter* **29**, 273002 (2017).

59. S. Smidstrup, A. Pedersen, K. Stokbro, H. Jónsson, Improved initial guess for minimum energy path calculations. *J. Chem. Phys.* **140**, 214106 (2014).

60. S. Plimpton, Fast Parallel Algorithms for Short-Range Molecular Dynamics. *Journal of Computational Physics* **117**, 1–19 (1995).

61. A. C. T. van Duin, S. Dasgupta, F. Lorant, W. A. Goddard, ReaxFF: A Reactive Force Field for Hydrocarbons. *J. Phys. Chem. A* **105**, 9396–9409 (2001).

62. L. Verlet, Computer “Experiments” on Classical Fluids. I. Thermodynamical Properties of Lennard-Jones Molecules. *Phys. Rev.* **159**, 98–103 (1967).
63. S. Nosé, A molecular dynamics method for simulations in the canonical ensemble. *Molecular Physics* **52**, 255–268 (1984).
64. W. G. Hoover, Canonical dynamics: Equilibrium phase-space distributions. *Phys. Rev. A* **31**, 1695–1697 (1985).
65. J. D. Weeks, D. Chandler, H. C. Andersen, Role of Repulsive Forces in Determining the Equilibrium Structure of Simple Liquids. *J. Chem. Phys.* **54**, 5237–5247 (1971).
66. A. Ahmed, R. J. Sadus, Phase diagram of the Weeks-Chandler-Andersen potential from very low to high temperatures and pressures. *Phys. Rev. E* **80**, 061101 (2009).